

# A method for reconstructing the Galactic magnetic field using dispersion of fast radio bursts and Faraday rotation of radio galaxies

A. Pandhi<sup>1,2</sup>, S. Hutschenreuter<sup>3</sup>, J. L. West<sup>2</sup>, B. M. Gaensler<sup>2,1</sup>, A. Stock<sup>1,4</sup>

<sup>1</sup>David A. Dunlap Department of Astronomy and Astrophysics, University of Toronto, 50 St. George Street, Toronto, ON M5S 3H4, Canada

<sup>2</sup>Dunlap Institute for Astronomy and Astrophysics, University of Toronto, 50 St. George Street, Toronto, ON M5S 3H4, Canada

<sup>3</sup>Department of Astrophysics/IMAPP, Radboud University Nijmegen; P.O. Box 9010, 6500 GL Nijmegen, Netherlands

<sup>4</sup>Canadian Institute for Theoretical Astrophysics, University of Toronto, 60 St. George Street, Toronto, ON, M5S 3H8, Canada

16 August 2022

## ABSTRACT

With the rapid increase of fast radio burst (FRB) detections within the past few years, there is now a catalogue being developed for all-sky extragalactic dispersion measure (DM) observations in addition to the existing collection of all-sky extragalactic Faraday rotation measurements (RMs) of radio galaxies. We present a method of reconstructing all-sky information of the Galactic magnetic field component parallel to the line of sight,  $B_{\parallel}$ , using simulated observations of the RM and DM along lines of sight to radio galaxies and FRB populations, respectively. This technique is capable of distinguishing between different input Galactic magnetic field and thermal electron density models. Significant extragalactic contributions to the DM are the predominant impediment in accurately reconstructing the Galactic DM and  $\langle B_{\parallel} \rangle$  skies. We look at ways to improve the reconstruction by applying a filtering algorithm on the simulated DM lines of sight and we derive generalized corrections for DM observations at  $|b| > 10$  deg that help to disentangle Galactic and extragalactic DM contributions. Overall, we are able to reconstruct both large-scale Galactic structure and local features in the Milky Way's magnetic field from the assumed models. We discuss the application of this technique to future FRB observations and address possible differences between our simulated model and observed data, namely: adjusting the priors of the inference model, an unevenly distributed population of FRBs on the sky, and localized extragalactic DM structures.

**Key words:** ISM: magnetic fields – Galaxy: structure – fast radio bursts

## 1 INTRODUCTION

The large-scale Galactic magnetic field (GMF) is important for understanding various astrophysical processes in the Galaxy, such as the structure and properties of the turbulent interstellar medium (ISM), molecular cloud collapse, star formation, cosmic-ray acceleration and propagation (for reviews, see [Ferrière 2001](#); [Haverkorn 2015](#); [Jaffe 2019](#), and references therein). As such, modeling the GMF is an active field of research that utilizes a variety of observational tracers and analytical techniques to probe properties such as the orientation and magnitude of the magnetic field perpendicular,  $B_{\perp}$ , and parallel,  $B_{\parallel}$ , to the observer's line of sight (LOS). A summary of large-scale GMF tracers, their dependencies, pros, and cons is presented in Table 1 of [Jaffe \(2019\)](#).

As linearly polarized emission propagates through a magnetized medium, free electrons along the LOS induce Faraday rotation of the observed radio emission. This effect is characterized by a difference in the measured polarization angle between two observing frequencies and is proportional to the square of the observing wavelength,  $\lambda^2$ . The observed polarization position angle,  $\chi(\lambda^2)$ , from a background source with an intrinsic polarization angle,  $\chi_0$ , and

Rotation Measure (RM) is described as:

$$\chi(\lambda^2) = \chi_0 + \text{RM}\lambda^2. \quad (1)$$

RM is in turn related to the integrated number density of electrons and parallel component of the magnetic field along the LOS:

$$\text{RM} = 0.812 \text{ rad m}^{-2} \int_0^d \left[ \frac{n_e(s)}{\text{cm}^{-3}} \right] \left[ \frac{B_{\parallel}(s)}{\mu\text{G}} \right] \left( \frac{ds}{\text{pc}} \right), \quad (2)$$

where  $n_e$  is the thermal electron density,  $d$  is the distance to the emitting source, and we define our limits of integration in accordance with [Ferrière et al. \(2021\)](#) such that we integrate from the source ( $s = 0$ ) to the observer ( $s = d$ ). Simultaneously, the emission is also dispersed by the free electrons. Empirically, this manifests as a wavelength dependent time delay of the observed emission which is parameterized by the dispersion measure (DM):

$$\text{DM} = \int_0^d \left[ \frac{n_e(s)}{\text{cm}^{-3}} \right] \left( \frac{ds}{\text{pc}} \right). \quad (3)$$

Note that equations 2 and 3 assume a cosmological redshift of zero; later in Section 2 we will explore RM and DM measurements

for extragalactic sources and their redshift dependence. The ratio between RM and DM, along the same LOS, provides an estimate of the electron density weighted average magnetic field strength parallel to the LOS:

$$\langle B_{\parallel} \rangle = \frac{\int_0^d n_e B_{\parallel} ds}{\int_0^d n_e ds} = 1.232 \mu\text{G} \left( \frac{\text{RM}}{\text{rad m}^{-2}} \right) \left( \frac{\text{DM}}{\text{pc cm}^{-3}} \right)^{-1}. \quad (4)$$

The mean direction of  $\langle B_{\parallel} \rangle$  is determined by positive (towards the observer) and negative (away from the observer) measurements of RM. The underlying assumption behind equation 4 is that the thermal electron density is uncorrelated with the LOS component of the magnetic field. However, this assumption may break down under certain circumstances, particularly at sub-kpc scales (see Beck et al. 2003; Seta & Federrath 2021).

RMs of polarized radio sources, in conjunction with DM, are therefore an effective method for probing the strength and direction of the parallel component of the magnetic field,  $\langle B_{\parallel} \rangle$ , in the intervening structure along the observed LOS. This technique has been widely used for sampling the 3D structure within the Galaxy using DMs and RMs of pulsars (e.g. Manchester 1972, 1974; Rand & Lyne 1994; Han et al. 1999; Noutsos et al. 2008; Sobey et al. 2019; Ng et al. 2020). Observed Galactic pulsar RMs provide 3D information within the Galaxy to the extent that we know the distance to the pulsar but the overall sampling is limited (currently 1320 observed pulsars have measured RMs) (ATNF Pulsar Catalogue V1.66: Manchester et al. 2005). Other studies have also created full-sky RM maps using polarized extragalactic radio sources (e.g. Oppermann et al. 2012, 2015; Hutschenreuter & Enßlin 2020; Hutschenreuter et al. 2022) without corresponding DM observations. The collection of extragalactic RMs is considerably larger than the sample of Galactic pulsar RMs, currently over 50000 sources<sup>1</sup>, primarily from observations of radio galaxies (Van Eck et al. in prep), and is well sampled over almost all lines of sight (although it loses the 3D information since all observations probe the full extent of the Galactic structure along the LOS). In particular, Oppermann et al. (2012, 2015) combined several extragalactic RM catalogues to reconstruct a full-sky map of observed total RM through the Galaxy, taking into account the uncertainties in the noise statistics. Following up on this work, Hutschenreuter & Enßlin (2020); Hutschenreuter et al. (2022) use an updated inference algorithm and incorporate the electron emission measure (EM) observed by the *Planck* survey (Planck Collaboration et al. 2016a,c) to produce updated maps of the Galactic RM. Both Galactic and extragalactic RM data sets are expected to greatly improve as the Square Kilometre Array (SKA) and its associated pathfinder surveys come online (e.g. Keane et al. 2015; Johnston-Hollitt et al. 2015; Heald et al. 2020).

The study of DMs, however, has been predominantly limited to Galactic sources, namely pulsar observations (currently 3160 observed pulsars have DMs measured) (ATNF Pulsar Catalogue V1.66: Manchester et al. 2005). Pulsars are transient sources on approximately millisecond to second timescales, allowing us to measure their DM. This is not the case for radio galaxies, which are continuously emitting at radio frequencies on these short timescales (Hales et al. 2016). Thus, there had not been a set of extragalactic DM data comparable in sky density to the extragalactic RM catalogue from radio galaxies, until the discovery of fast radio bursts (FRBs). FRBs are millisecond-duration radio transients that were

first identified in 2007, when Lorimer et al. (2007) detected a 30 Jy radio burst with a  $< 5$  ms duration using data from the Parkes radio telescope. The observation and localization of FRBs has become a rapidly growing field, with the Canadian Hydrogen Intensity Mapping Experiment Fast Radio Burst (CHIME/FRB) Project recently releasing a catalogue of 536 FRBs (CHIME/FRB Collaboration et al. 2021). The inferred sky rate of FRB events at 1.4 GHz with a fluence above 3 – 4 Jy ms is estimated between several hundred and a few thousand per sky per day (e.g. Thornton et al. 2013; Rane et al. 2016; Lawrence et al. 2017), implying that there is still a wealth of observational data to come in the future.

This expanding catalogue of FRBs<sup>2</sup> presents a large source of extragalactic DM observations that we cannot obtain using radio galaxies. While FRBs also provide RMs (McKinven et al. 2021), the total number of observed FRBs is much smaller than the available RM sample from radio galaxies. Thus, FRB RMs will not be considered in this work. While there is no consensus as to the specific origin and physical mechanisms behind FRBs (for a review, see Platts et al. 2019; Cordes & Chatterjee 2019), measurements of their DMs (typically hundreds of  $\text{pc cm}^{-3}$ ) are too large to be entirely accredited to Milky Way (MW) contributions and are consistent with extragalactic origins. Additionally, several FRBs have been localized to other galaxies (e.g. Chatterjee et al. 2017; Ravi et al. 2019; Bannister et al. 2019; Marcote et al. 2020).

In general, the observed DM from an extragalactic source,  $\text{DM}_{\text{obs}}$  can be separated into distinct contributing components:

$$\text{DM}_{\text{obs}} = \text{DM}_{\text{disk}} + \text{DM}_{\text{halo}} + \text{DM}_{\text{IGM}} + \text{DM}_{\text{host}}, \quad (5)$$

where  $\text{DM}_{\text{disk}}$  is contribution from warm ionized gas in the MW disk ( $T \lesssim 10^4$  K),  $\text{DM}_{\text{halo}}$  is from the extended hot Galactic halo ( $T \sim 10^6 - 10^7$  K),  $\text{DM}_{\text{IGM}}$  is contributions from the intergalactic medium and intervening systems, and  $\text{DM}_{\text{host}}$  is from the host galaxy of the source and its local environment (Yamasaki & Totani 2020, and references therein). Similarly, the  $\text{RM}_{\text{obs}}$  is also broken down into a Galactic component (disk and halo) and extragalactic contributions, which are in general much smaller than the Galactic component:

$$\text{RM}_{\text{obs}} = \text{RM}_{\text{disk}} + \text{RM}_{\text{halo}} + \text{RM}_{\text{xgal}}, \quad (6)$$

Importantly, in equation 6, the sum of all extragalactic RM contributions is folded into  $\text{RM}_{\text{xgal}}$  rather than explicitly including  $\text{RM}_{\text{IGM}}$  and  $\text{RM}_{\text{host}}$  terms. This distinction is further examined in Section 2, which also includes a more detailed breakdown of the DM and RM contributions and estimates.

With the aforementioned growing FRB catalogue, the proposition of studying the full DM sky using methods similar to Oppermann et al. (2012, 2015) and Hutschenreuter & Enßlin (2020) becomes increasingly plausible. With full-sky information of both RM and DM, one could, in principle, apply equation 4 to reconstruct an approximation of the  $\langle B_{\parallel} \rangle$  sky. In this work, we propose to establish and test a robust method of reconstructing  $\langle B_{\parallel} \rangle$  information across the sky using simulated data. Specifically, this will be done by assuming an underlying model of the GMF (e.g. Sun & Reich 2010; Jansson & Farrar 2012; Jaffe et al. 2013; Terral & Ferrière 2017) and  $n_e$  (e.g. Yao et al. 2017; Yamasaki & Totani 2020). Then, we simulate a distribution of FRB and radio galaxy populations with associated DM and RM contributions, respectively. By applying a reasonable lower limit to the observed flux from FRBs and determining the LOS and distance to these simulated points,

<sup>1</sup> An up to date RM catalogue is at <https://github.com/CIRADA-Tools/RMTable>.

<sup>2</sup> An up to date catalogue of FRB observations is at <https://hertexperiment.org/frbstats>.



we can recreate the conditions for typical extragalactic FRB and radio galaxy observations. Consequently, we use the simulated observations to build up approximations of the DM and RM skies with a joint inference algorithm and use these to reconstruct a map of the simulated  $\langle B_{\parallel} \rangle$  across the sky. By contrasting the resulting reconstruction with the underlying GMF model, we determine the validity and accuracy of the technique. Stemming from this analysis, we further explore methods of handling DM observations and correcting for the significant extragalactic contributions that naturally arise.

The remainder of this paper is structured as follows. In Section 2 we discuss the details of generating observables from underlying assumptions of the GMF and  $n_e$  distribution and simulating FRB and radio galaxy populations. Section 3 illustrates the use of Information Field Theory (IFT) (Enßlin et al. 2009; Enßlin 2019), which incorporates methods from Bayesian statistics and statistical field theory, to infer underlying continuous fields from noisy incomplete data. The results of the joint inference and data reduction techniques utilized to minimize the extragalactic DM contributions are presented in Section 4. In Section 5 we derive a correction factor to further reduce extragalactic DM and discuss the implications of our work.

## 2 SIMULATED OBSERVATIONS

This section details the various steps taken to create our simulated DM and RM observations. These steps are summarized as a flowchart in Figure 1.

### 2.1 HammurabiX & Input Models

The *hammurabiX*<sup>3</sup> (V2.4.1) package (Wang et al. 2020) is an open source astrophysical magnetic field simulator that incorporates user input 3D models of different components of the MW disk ISM and halo, such as magnetic fields, and thermal and relativistic electrons. Given input models for these components, the code utilizes the HEALPix library to execute efficient LOS integrals through the simulated 3D Galactic model by using multi-layered spherical shells with adaptable resolutions. *HammurabiX* integrates along the LOS to compute the synchrotron emission component of Stokes  $I$ ,  $Q$ , and  $U$ , and the Faraday depth and DM are then calculated from discrete forms of equations 2 and 3. For the purposes of this work, we utilize *hammurabiX* to generate simulated maps of RM and DM by inputting pre-existing models for the GMF and thermal electron density. Below, we discuss the specifics of the assumed models in this study; this collection of models was chosen because of their flexible implementation in *hammurabiX*, which allows for alterations to each model parameter.

For the GMF model, we adopt the formulation laid out by Jansson & Farrar (2012) (hereafter JF12). The JF12 model is comprised of: (i) a disk component between Galactic radii  $r$  of 3 kpc and 20 kpc, containing a purely azimuthal field at 3 kpc  $< r < 5$  kpc and eight logarithmic spiral regions beyond 5 kpc; (ii) a toroidal halo component with an exponential scale height and independent amplitudes parameters for the north and south sections of the field; (iii) an X-shaped poloidal halo component—which is not included in many other GMF models—replicating similar behaviour seen in radio observations of edge-on galaxies (e.g. Krause 2009; Beck 2009;

Krause et al. 2020). For a set of best-fit model parameters see Table 1 of Jansson & Farrar (2012).

The JF12 model was originally written in *hammurabi* (Waelkens et al. 2009), a predecessor to *hammurabiX*. The model was made available in the V2.4.1 release of *hammurabiX*. The coherent magnetic field is consistent in both implementations, although the *hammurabiX* implementation creates generally smoother maps due to changes in the numerical integration routines.

The thermal electron density model utilized in this work incorporates separate models for the disk component (Yao et al. 2017) (hereafter YMW16) and halo component (Yamasaki & Totani 2020) (hereafter YT20). YMW16 is made up of: (i) a thick disk representing the diffuse ionized medium; (ii) a thin disk which models the region of increased gas density and star formation a few kpc out from the Galactic center, dubbed the "molecular ring"; (iii) the Galactic center; (iv) a set of spiral arms (for specific spiral-arm parameters see Table 1 of Yao et al. 2017); (v) various local features (e.g. the Gum Nebula or Local Bubble). For this work, we elect to remove the Gum Nebula from the model as its implementation within *hammurabiX* (V2.4.1) creates unintended sharp features in the on-sky projection of key observables, such as RM and DM, that are unphysical. We note that the choice to remove the Gum Nebula from the model has no impact on this study and its results. In regards to the halo model, YT20 is a sum of two exponential components, a compact disk-like component and an extended spherical halo.

### 2.2 Simulating Radio Galaxy & FRB Populations

To simulate LOS RM and DM observations, we require a method of generating typical radio galaxy and FRB populations, respectively. To obtain a population of radio galaxies in line with current understanding and observations, we take advantage of the aforementioned catalogue of extragalactic point sources (Van Eck et al. in prep; V0.2.1). However, the simulated LOS observables will be determined by the assumed field models and thus we only extract the on-sky positions, in both celestial and Galactic coordinates systems, along with measured RM errors. The measured RM itself is not taken from the pre-existing catalogue and will be evaluated in a later step based on equation 2 and assumed GMF and  $n_e$  models. Moreover, any known pulsars (35 out of 50207 entries) and data points without a reported RM error (71 out of 50207 entries) are removed from the sample. The remaining 50101 point sources comprise our radio galaxy population and are plotted with respect to their measured RA, DEC, and  $RM_{\text{err}}$  in Figure 2.

The *frbpoppy*<sup>4</sup> (V2.1.0) package is a tool for conducting FRB population synthesis (Gardenier et al. 2019). Our goal with this package is to generate a simulated sample of FRBs that would be realistically observable by current radio instruments. Typically, assuming a 1 ms burst duration, observed FRBs have luminosities on the order of  $\sim 10^8 - 10^9 L_{\odot}$  (or  $\sim 10^{41} - 10^{42}$  erg s<sup>-1</sup>) (see Figure 2 of CHIME/FRB Collaboration et al. 2020) and are inferred to be occurring in galaxies with a cosmological distance scale,  $z \sim 1$  (Yamasaki & Totani 2020). Therefore, we utilize *frbpoppy* to generate three independent sets of populations with roughly 1000, 10000, and 50000 observable FRBs each. The varying sized datasets enable us to analyze the ability of our joint inference technique to produce accurate results with increasingly larger samples of FRBs. Likewise, the range of population sizes encompasses the approximate number of FRB observations available within the next few years and

<sup>3</sup> <https://github.com/hammurabi-dev/hammurabiX>

<sup>4</sup> <https://github.com/davidgardenier/frbpoppy>

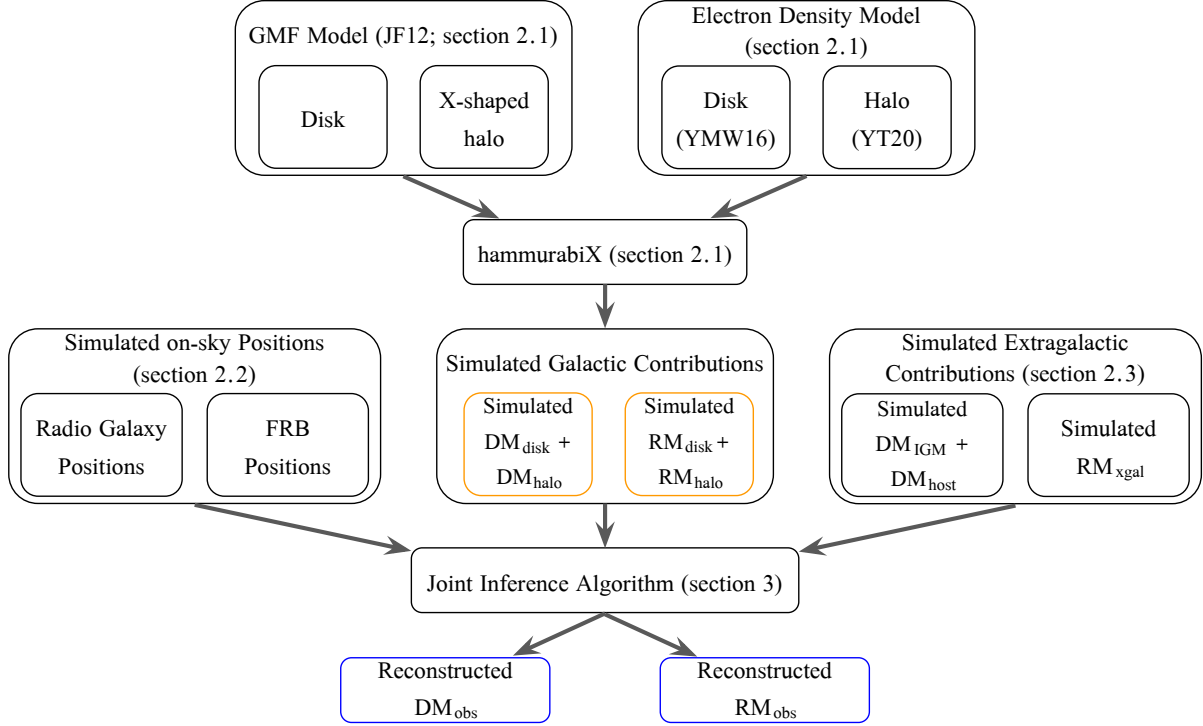


**Figure 1.** A flowchart summarizing the assumed models, methods, and outputs of our simulated data generation process (section 2) and the joint inference algorithm (section 3). DM and RM components follow the same breakdown as equations 5 and 6. We highlight the Galactic maps we are attempting to recreate in orange and the reconstruction results in blue. Note that  $\langle B_{\parallel} \rangle$  is not a direct output of `hamurabiX` or the joint inference algorithm and is instead computed from the RM and DM by using equation 4.

up to the stage where they are commensurate with the current RM catalogue. The population is distributed over a conservative range of redshifts  $0 < z < 2$  and luminosities  $10^{40} \text{ erg s}^{-1} < L < 10^{45} \text{ erg s}^{-1}$  bracketing the typical quantities from Yamasaki & Totani (2020) and CHIME/FRB Collaboration et al. (2020), respectively. FRB luminosities are drawn from a uniform distribution spanning this range. We follow the default FRB spectral index and pulse width distributions provided in `frbpoppy`. The spectral index  $\gamma$  follows a Gaussian distribution with mean  $\bar{\gamma} = -1.4$  and standard deviation  $\sigma_{\gamma} = 1$  (Gardenier et al. 2019, and references therein). Meanwhile, the FRB pulse width  $w$  follows a uniform distribution spanning  $0 \text{ ms} < w < 10 \text{ ms}$ . It should be noted that there are a number of effects that modify the pulse width before it is measured on Earth; for a detailed discussion of these effects see Section 3 of Gardenier et al. (2019). Additionally, we assume a uniform distribution of sources on the sky and a constant number density of sources per comoving volume.

Next, we apply a filtering criterion to the FRB population with respect to a selected instrument or survey to draw out a sub-sample of FRBs that would be realistically observable. Since the CHIME/FRB project has, so far, collated the largest set of FRB data, we elect to use a filter that resembles CHIME/FRB specifications. While the exact survey design of CHIME is complicated and difficult to replicate, a simple version of its system parameters is implemented into `frbpoppy`. Here, we present a list of some relevant parameters (for a full list of parameters, see <https://github.com/davidgardenier/frbpoppy>): frequency range: 400–800 MHz, receiver temperature: 50 K, sampling time: 1 ms, integration time: 360 s, and detection threshold signal-to-noise ratio: 10. In reality, the sky distribution of CHIME/FRB observations

ranges between approximately  $-11 \text{ deg} < \text{DEC} < 90 \text{ deg}$  and is not uniformly distributed due to variations in source transit duration as a function of declination (CHIME/FRB Collaboration et al. 2018, 2021). Additionally, the sensitivity of the observations also varies with declination. However, in this work we do not attempt to replicate the sky distribution of CHIME/FRB sources but rather generate a set of full sky simulated observations that is representative of typical FRB observations. Consequently, we apply this filter over the full range of RA and DEC and maintain a uniform sky distribution of simulated sources. An example of a generated FRB population, with a total of 100000 sources, is plotted in Figure 2. In this example, approximately 1.3% of the total population successfully pass the filtering criteria and are overplotted as blue markers.

### 2.3 Simulating LOS Observations

With the radio galaxy and FRB populations in place, we must now account for the DM and RM contributions from Galactic and extragalactic components of the foreground sight-lines. For most extragalactic RM sources, the net polarization angle rotation is dominated by effects originating from the MW’s ISM (e.g. Schnitzeler 2010; Oppermann et al. 2015). Schnitzeler (2010) modelled the width of the RM distribution,  $\sigma_{\text{RM}}$ , for NVSS RM catalogue sources as a dominant Galactic contribution ( $\bar{\sigma}_{\text{RM,MW}} \sim 8 \text{ rad m}^{-2}$ ) that is amplified at smaller Galactic latitudes as  $1/|\sin|b||$  and a small extragalactic component ( $\bar{\sigma}_{\text{RM,EG}} \sim 6 \text{ rad m}^{-2}$ ) independent of Galactic latitude:  $\sigma_{\text{RM}}(b)^2 = \left( \frac{\bar{\sigma}_{\text{RM,MW}}}{\sin|b|} \right)^2 + \bar{\sigma}_{\text{RM,EG}}^2$ . Furthermore, Oppermann et al. (2015) estimate the contribution from non-Galactic media using a statistical noise model (for a detailed discussion of

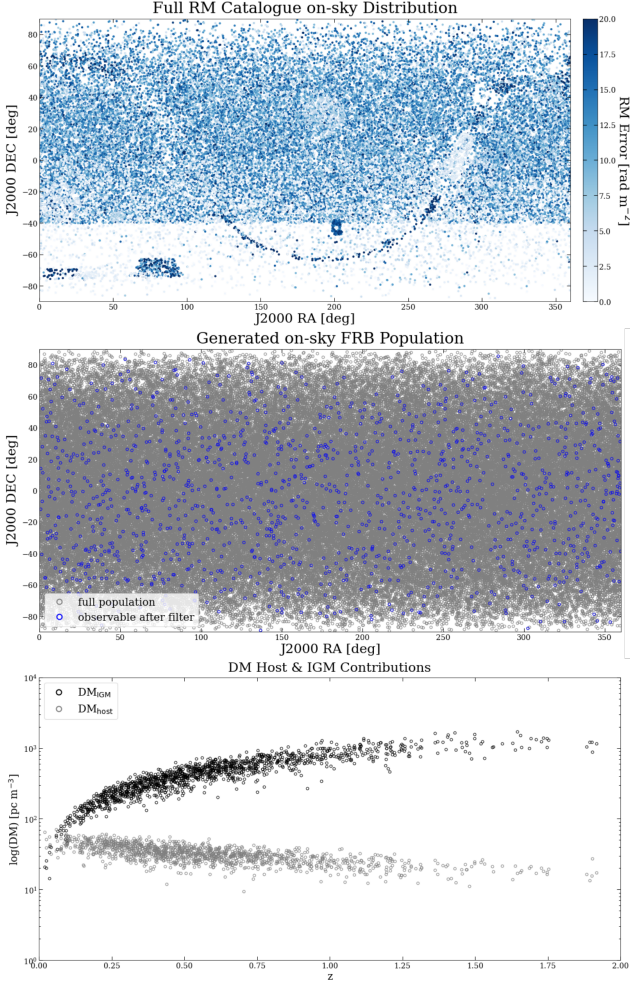


**Figure 2.** A projection of the assumed radio galaxy and FRB populations in J2000 celestial coordinates and a breakdown of the assumed extragalactic DM model. (Top) The on-sky distribution of the assumed radio galaxy population in this work. In total there are 50101 extragalactic point sources that are colored as a function of the corresponding error in RM measurements. (Middle) The on-sky distribution of the generated FRB population spanning redshifts  $0 < z < 2$ . Grey points represent the total generated populations (100000 sources) and the blue points are the sub-sample that pass our filter (1308 sources). (Bottom) Contributions to the total observed DM along a given LOS from extragalactic sources as a function of redshift. Contribution from host galaxies are plotted as grey points while black points correspond to the IGM contribution.

the noise model see section 2.3.2 of [Hutsenreuter & Enßlin \(2020\)](#). The fundamental idea of this process is to use on-sky correlations as the basis for discriminators between Galactic and extragalactic contribution. Based on this formulation, [Oppermann et al. \(2015\)](#) place an upper limit on the standard deviation of extragalactic Faraday depth contribution at  $\sigma_{\text{RM,EG}} \sim 7 \text{ rad m}^{-2}$ . Their result is in close agreement with [Schnitzler \(2010\)](#) and shows that the Galactic component is largely dominant in RM observations. Conceptually, this stems from the  $B_{\parallel}$  dependence seen in equation 2 which is not always pointed in the same direction along the entire path length and can often reverse along the LOS when the path length is much larger than the magnetic field scales (e.g. in the case of extragalactic sources). This is not the case for extragalactic DM contributions because the integral of  $n_e$  is a monotonically increasing function of distance.

In this work, the Galactic RM contribution along a given LOS is computed as a simulated observable from `hammurabiX`, assuming the combination of previously discussed models (YMW16, YT20, and JF12). We independently incorporate an extragalactic component by sampling from a normal distribution centered at zero with a standard deviation of  $\sigma_{\text{RM,EG}} = 7 \text{ rad m}^{-2}$  for each simulated LOS observation.

Similarly, the Galactic ISM and halo components of DM are output from `hammurabiX`, derived from the input  $n_e$  models (YMW16 and YT20). However, in the case of DM, there is significant contributions from the host galaxy,  $\text{DM}_{\text{host}}$ , and IGM,  $\text{DM}_{\text{IGM}}$ . In this regard, we follow the procedure described by [Macquart et al. \(2020\)](#), who find that  $\text{DM}_{\text{IGM}}$  is expected to have a strong redshift dependence, while the value of  $\text{DM}_{\text{host}}$  as observed from Earth is weighted by  $(1 + z_{\text{FRB}})^{-1}$ . In particular, these quantities are approximated as:

$$\text{DM}_{\text{host}} = 50(1 + z_{\text{FRB}})^{-1} \text{ pc cm}^{-3}, \quad (7)$$

$$\langle \text{DM}_{\text{IGM}} \rangle = \int_0^{z_{\text{FRB}}} \frac{c\tilde{n}_e(z)dz}{H_0(1+z)^2\sqrt{\Omega_m(1+z)^3 + \Omega_\Lambda}}, \quad (8)$$

where  $\tilde{n}_e = f_d \rho_b(z) m_p^{-1} (1 - Y_{\text{He}}/2)$ , with proton mass  $m_p$ , helium mass fraction  $Y_{\text{He}}$  that is assumed to be doubly ionized, the fraction of cosmic baryons in diffuse ionized gas  $f_d(z)$ ,  $\Omega_m$  and  $\Omega_\Lambda$  are the current matter and dark energy densities of the Universe, respectively, and  $\rho_b(z) = \Omega_b \rho_{c,0} (1+z)^3$  with  $\rho_{c,0} = 3H_0^2/8\pi G$ . For the subset of arcsecond and sub-arcsecond localized FRBs, this leads to an empirical relationship between  $\text{DM}_{\text{IGM}}$  and  $z$ , dubbed the “Macquart relation” (see Figure 2 from [Macquart et al. 2020](#)). In their analysis, the estimated DM contribution from the MW and the FRB host galaxy has been subtracted from  $\text{DM}_{\text{obs}}$ . The localized FRB sample is in agreement with the expected  $\text{DM}_{\text{IGM}} - z$  relation (see equation 8) for *Planck* 15 cosmology (i.e.  $\Omega_b = 0.0486$  and  $H_0 = 67.74 \text{ km s}^{-1} \text{ Mpc}^{-1}$ ) ([Planck Collaboration et al. 2016b](#)) after accounting for the scatter from the IGM.

In this work, we adopt the formalism described above to determine the extragalactic contribution to  $\text{DM}_{\text{obs}}$ . Namely,  $\text{DM}_{\text{host}}$  follows a Gaussian model with the mean being equivalent to equation 7 and a standard deviation of  $\sigma_{\text{DM,host}} = 10(1 + z_{\text{FRB}})^{-1} \text{ pc cm}^{-3}$ . Similarly, we model our IGM contribution to follow the linear  $\text{DM}_{\text{IGM}} - z$  relation derived from equation 8 with a 20% spread as a function of redshift (i.e.  $\sigma_{\text{DM,IGM}} = 0.2 \langle \text{DM}_{\text{IGM}} \rangle (z) \text{ pc cm}^{-3}$ ). For the same example population of observable FRBs shown in the second panel of Figure 2, we plot the distribution of simulated  $\text{DM}_{\text{host}}$  and  $\text{DM}_{\text{IGM}}$  contributions as a function of redshift in the final panel of Figure 2. There are examples in literature of studies that examine additional sources of extragalactic DM contributions. For example, [Prochaska & Zheng \(2019\)](#) study DM contributions from the highly ionized Local Group Medium (LGM) and generate sky-projection maps of the  $\text{DM}_{\text{LGM}}$  and DM contribution from M31 and the Magellanic Clouds. However, in this work we do not include these components and rather consider a simple model in which the extragalactic DM is built up entirely from contributions from the host galaxy and IGM.

### 3 JOINT INFERENCE RECONSTRUCTION

In this section, we describe the joint inference setup to reconstruct the Galactic RM and DM skies from extragalactic point source measurements. Depending on their location and density on the sky,



these data sets probe the Galactic sky on various scales and environments. Our a priori knowledge, especially on the Galactic DM sky, is rather limited and usually constrained to the largest scales (e.g. see [Cordes & Lazio 2002](#); [Yao et al. 2017](#)) or along specific LOS constrained by pulsars. This means we have no reliable parametric model at hand that we can expect to be an accurate representation of the underlying field on all scales and locations probed by our data sets. Hence, we opt to infer both skies non-parametrically by utilizing generic models with a large number of degrees of freedom that are only constrained by the data and generic assumptions on smoothness and the expected range of values. This is done by formulating the problem within IFT, a Bayesian inference framework useful for high dimensional problems ([Enßlin 2019](#)). The resulting posterior distribution, which, depending on the resolution of the sky maps, can have millions of degrees of freedom, is evaluated using a variational Bayesian optimization scheme called Metric Gaussian Variational Inference ([Knollmüller & Enßlin 2019](#)).

In the next paragraphs, we summarize the components of our model that are specific to this work. We start our description by connecting the data  $d_s$  (with  $s \in \{\text{RM}, \text{DM}\}$ ) to the respective Galactic sky maps  $s_{\text{gal}}$ , which are defined on a HEALPix ([Górski et al. 2005](#)) grid on the unit sphere,

$$d_s = \mathcal{R}s_{\text{gal}} + \mathcal{R}s_{\text{xgal}} + n_s, \quad (9)$$

where  $\mathcal{R}$  is a projection operator on the data vector,  $s_{\text{xgal}}$  describes the extragalactic component, and  $n_s$  is the observational noise. The latter is assumed to be drawn from a zero mean Gaussian with known diagonal covariance  $\sigma_{d_s}^2$ . At this point, we can identify three issues, which need to be addressed in our modeling:

- (i) While we are interested in  $s_{\text{gal}}$ , equation 9 is usually not invertible even in the noiseless case (i.e. not every pixel of the sky maps will be constrained by data). Thus, we need to infer an interpolation kernel that is able to constrain pixels by exploiting correlations of nearby data points;
- (ii) The extragalactic contribution, particularly in DM, is often as strong as or stronger than the Galactic component. Therefore, we require a method of constraining and separating the extragalactic contributions to better estimate the Galactic structure;
- (iii) We need a physically plausible inference model for both  $\text{RM}_{\text{gal}}$  and  $\text{DM}_{\text{gal}}$ , which is capable of representing known large scale features, such as the Galactic disk, but is also flexible enough to characterize unknown structures hidden in the data. The model should furthermore be able to efficiently exploit the correlations between the RM and DM maps.

Issue (i) touches on an integral feature of IFT and the Numerical Information Field Theory Python package (NIFTy) ([Arras et al. 2019](#)), namely the modeling of correlations. We parameterize each sky map as a non-linear combination of Gaussian sky maps, which have a parametrizable correlation structure in terms of power spectra. For the details of the power spectrum modeling we refer the reader to [Arras et al. \(2022\)](#).

In regard to issue (ii), we refrain from explicitly modelling the extragalactic component (for both RM and DM) in the inference but instead take several steps to minimize the effects of extragalactic contribution on the reconstructed results by means of data reduction and the derivation of a correction factor. For a detailed discussion of these steps, see Sections 4 and 5, respectively.

Finally, regarding issue (iii), the modeling of the Galactic RM and DM skies needs to be discussed. For the RM sky, we follow the recipe of [Hutschenreuter & Enßlin \(2020\)](#) and [Hutschenreuter et al.](#)

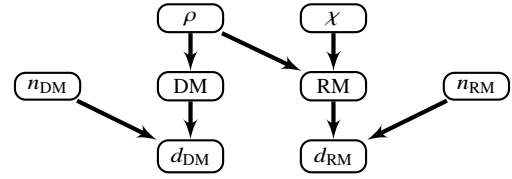


**Figure 3.** A simplified model tree for the joint RM/DM inference scheme. In reality, there exist several layers above the  $\rho$  and  $\chi$  nodes pertaining to the implicit correlation structure modeling.

(2022) and model the map as a combination of two components,

$$\text{RM}_{\text{gal}} = 0.812e^\rho \chi. \quad (10)$$

Both  $\rho$  and  $\chi$  are Gaussian sky maps with a priori unknown power spectra. This is mostly motivated by the need to model both strong variations in RM amplitude (mostly via the log-normal  $\rho$  map), and the sign of the RM sky (via the  $\chi$  map). This models ties back in to equation 4 insofar as the thermal electron density and magnetic field vector are uncorrelated. In this case,  $e^\rho$  might be viewed as a proxy for the morphology of the DM sky, which dominates the sky structure of the RM amplitude ([Hutschenreuter & Enßlin 2020](#)). Similarly, the  $\chi$  map can then be seen as a proxy for the averaged magnetic field sky, as amplitude structures correlated with the sign are most likely also represented in this map and under the assumption that these are then most likely caused by the magnetic field. Unfortunately, no further conclusions on absolute scales or the reliability of specific structures can be drawn due to degeneracy between the two maps, if the model is constrained using RM data only as in [Hutschenreuter et al. \(2022\)](#). However, this changes if we add the DM data to constrain the amplitude field by assuming,

$$\text{DM}_{\text{gal}} = e^\rho, \quad (11)$$

as a model for the DM sky, which is also proposed by [Hutschenreuter \(in prep\)](#). As the DM map is also parametrized by  $\rho$ , both sky maps are now connected in the inference and any change in either map will immediately be reflected in the other. From this it follows that, if we assume no correlations between  $n_e$  and  $B_{\parallel}$ , the posterior  $\chi$  map should represent our best estimate on the averaged LOS component of the GMF. The corresponding hierarchical tree of this joint inference model is depicted in Figure 3. The inference algorithm is implemented in NIFTy version 7.

## 4 RESULTS

The results of the joint inference reconstruction for various input models and testing are presented throughout this section. All on-sky maps are presented in the form of HEALPix Mollweide projections with  $\text{nside} = 128$  (i.e. with a total of 196608 pixels or, equivalently, a resolution of  $\sim 27.5$  arcminutes) and in Galactic coordinates. The reconstructed maps are directly compared to the underlying fields by way of contrasting against the all-sky `hammurabiX` outputs for DM, RM, and  $\langle B_{\parallel} \rangle$ . This method of analysis tests not only the accuracy of the reconstruction but also how well we are able to disentangle the Galactic and extragalactic contributions from the simulated observations. The key results are included in this section, but complete reconstruction information, including corresponding reconstruction errors, are located in Appendix A.



#### 4.1 Baseline Galactic Model

To test the capability of the reconstruction algorithm, independently of how well we can constrain the extragalactic component of the observables, we begin by applying the algorithm to a set of data that contains only the Galactic information along each LOS. The extragalactic component is explicitly set to zero at each LOS; while this is unphysical, it will provide a useful baseline for the best possible reconstruction results. Each column of Figure 4 contains the on-sky DM, RM, and  $\langle B_{\parallel} \rangle$  (computed according to equations 2, 3, and 4) information, respectively. The first row shows the *hammurabiX* outputs based on our assumed Galactic models and each consequent row presents the reconstructed map of each observable for varying sized data sets. As was mentioned in Section 2, unlike the FRB population, the radio galaxy population that we have adapted in this study has a fixed size and therefore we only present the RM reconstruction for one run of the joint inference algorithm. The changes in the RM reconstruction are negligible as we vary the size of the FRB population between runs. From Figure 4 alone, it can be difficult to see the differences between the reconstruction results and the corresponding *hammurabiX* output. To quantitatively measure these differences, we analyze the accuracy of the reconstruction results below. In addition, we generate plots of the DM maps in a log base 10 scale (to better visualize low-DM regions away from the Galactic plane) and provide difference maps for the RM and  $\langle B_{\parallel} \rangle$  reconstructions in Appendix A.

With a population of radio galaxies distributed identically to that of the observed sample, we are able to reconstruct the RM-sky to an extremely high degree of precision. The DM reconstruction for 50000 FRBs is also largely in good agreement with the expected DM-sky. Especially with regard to characterizing the shape of the large scale structure in the Galactic plane (for example the high DM closer to the Galactic centre (GC) followed by lower DMs away from the GC) the algorithm performs exceptionally. In the outer regions of the disk ( $60 \text{ deg} \leq \ell \leq 300 \text{ deg}$ ), the absolute difference between the reconstructed DM and the *hammurabiX* map is  $\lesssim 20 \text{ pc cm}^{-3}$ . The largest discrepancy is in approximating the magnitude of the DM in the Galactic plane near the GC. Here, the assumed  $n_e$  model has DMs  $\gtrsim 10^3 \text{ pc cm}^{-3}$  uniformly in the plane but the joint inference algorithm appears to identify high DM simulated observations in this region as localized structure. Therefore, the reconstructed map underestimates the DM by  $\sim 10^2 - 10^3 \text{ pc cm}^{-3}$  in small patches of the inner Galactic plane ( $|b| \lesssim 5 \text{ deg}$ ,  $\ell \lesssim 60 \text{ deg}$  and  $\ell \gtrsim 300 \text{ deg}$ ). Local features, such as spiral arms manifesting as roughly circular over-densities in the disk, are also easily identifiable in the reconstruction. Moving off the Galactic plane, the reconstruction agrees with the model to within  $\lesssim 5 \text{ pc cm}^{-3}$  (for  $5 \text{ deg} \leq |b| \leq 30 \text{ deg}$ ) and to within  $\lesssim 1 \text{ pc cm}^{-3}$  (for  $|b| > 30 \text{ deg}$ ).

As we move to smaller data sets (10000 and 1000 FRBs, respectively), the results maintain a lot of the large scale structure but the accuracy of the reconstruction begins to decline. In particular, with only 1000 data points, the coverage becomes patchy at points throughout the Galactic plane and the local features (spiral arms and the Loop I region) are difficult to recognize. Even in the outer regions of the Galactic plane, which were well estimated with the 50000 FRB sample, we begin to see DMs that differ from the *hammurabiX* output by  $\sim 10^2 \text{ pc cm}^{-3}$ . Off the plane, the 1000 FRB reconstruction differs from the *hammurabiX* output by  $\lesssim 12 \text{ pc cm}^{-3}$  (for  $5 \text{ deg} \leq |b| \leq 30 \text{ deg}$ ) and by  $\lesssim 2 \text{ pc cm}^{-3}$  (for  $|b| > 30 \text{ deg}$ ).

Following equation 4, the accuracy of the reconstructed  $\langle B_{\parallel} \rangle$ -sky is directly dependent on how well we are able to characterize the

DM and RM, respectively. Since the only significant discrepancies from the expected values are in the DM reconstruction, the accuracy of the  $\langle B_{\parallel} \rangle$  maps are reflective of the accuracy of the corresponding DM-sky and we observe the same trends with the 10000 and 1000 FRB reconstruction. For the 50000 FRB reconstruction, there were some small regions in the inner Galactic plane that were within  $\lesssim 0.3 \mu\text{G}$  of the corresponding *hammurabiX* map, but most of the Galactic plane and halo was within  $\lesssim 0.1 \mu\text{G}$ . At 1000 FRBs, the patchy coverage is again present (similar to the corresponding DM map) and we find discrepancies of  $\lesssim 0.3 \mu\text{G}$  from the expected value throughout most of the disk and  $\lesssim 0.15 \mu\text{G}$  in the halo.

#### 4.2 Full Model Reconstruction

Administering the joint inference algorithm on the full simulated LOS observations (now including the extragalactic contributions) drastically changes the results from the previous section. Dissimilar from what we see in RM, the extragalactic DM contribution is significant when compared to Galactic contributions from the MW's ISM and halo. The first two columns of Figure 5 show the reconstructed DM and  $\langle B_{\parallel} \rangle$  maps; similar to Figure 4, successive rows illustrate the results of the algorithm when applied to increasingly smaller FRB data sets. The reconstruction for 50000 FRBs shows a lot of the large scale Galactic DM structure visible in the corresponding panel of Figure 4 and local DM structure is still, to a lesser degree, discernible. However, the extragalactic components add a mean DM contribution of approximately  $300 \text{ pc cm}^{-3}$  to the reconstruction results that does not show any preferred structure as a function of Galactic coordinates and is generally isotropic. Thus, the sharp local features noted in the previous section are drowned out to an extent. For the smallest data set (1000 FRBs), where the algorithm must interpolate over larger areas of the sky that lack FRB data, the extragalactic contribution begins to appear weakly structured. However, we know that this extragalactic contribution should not be correlated over Galactic coordinates and it is therefore a sign that there are an insufficient number of data points for an accurate reconstruction, especially away from the Galactic plane. The overall effect of overestimating the Galactic DM due to extragalactic contributions translates to an underestimation of the parallel magnetic field component  $\langle B_{\parallel} \rangle$  (following equation 4), particularly at higher latitudes.

To reduce the aforementioned effects and recover more of the Galactic DM and  $\langle B_{\parallel} \rangle$  structure, we employ a technique to minimize the extragalactic DM in equal-area portions of the sky. To accomplish this, we utilize a low resolution Mollweide projection HEALPix grid, which divides the sky into equal-area sub-sections. For the largest simulated data set, we use a grid with  $n_{\text{side}} = 16$  (i.e. 3072 sub-sections with a mean spacing of  $3.6645 \text{ deg}$ ) and from all LOS observations encompassed in an individual sub-section, we only keep the single LOS with the minimum  $\text{DM}_{\text{tot}}$  (likely the nearest FRB with the lowest observed extragalactic DM contribution). Repeating this over the whole sky, our filtered FRB population then contains a total of 3072 data points that are roughly evenly distributed across the sky. The same process is used to filter the smaller populations, although the HEALPix grid resolution is decreased to  $n_{\text{side}} = 8$  (i.e. 768 sub-sections with a mean spacing of  $7.3290 \text{ deg}$ ) to compensate for the smaller data sets, and the filtered populations contain 768 (initially 10000) and 563 (initially 1000) FRBs, respectively. From the last two columns of Figure 5, we see that this step does improve both DM and  $\langle B_{\parallel} \rangle$  reconstructed maps and we better recover some of the local features of the Galactic structure. Specifically, the mean DM contribution from extragalactic sources

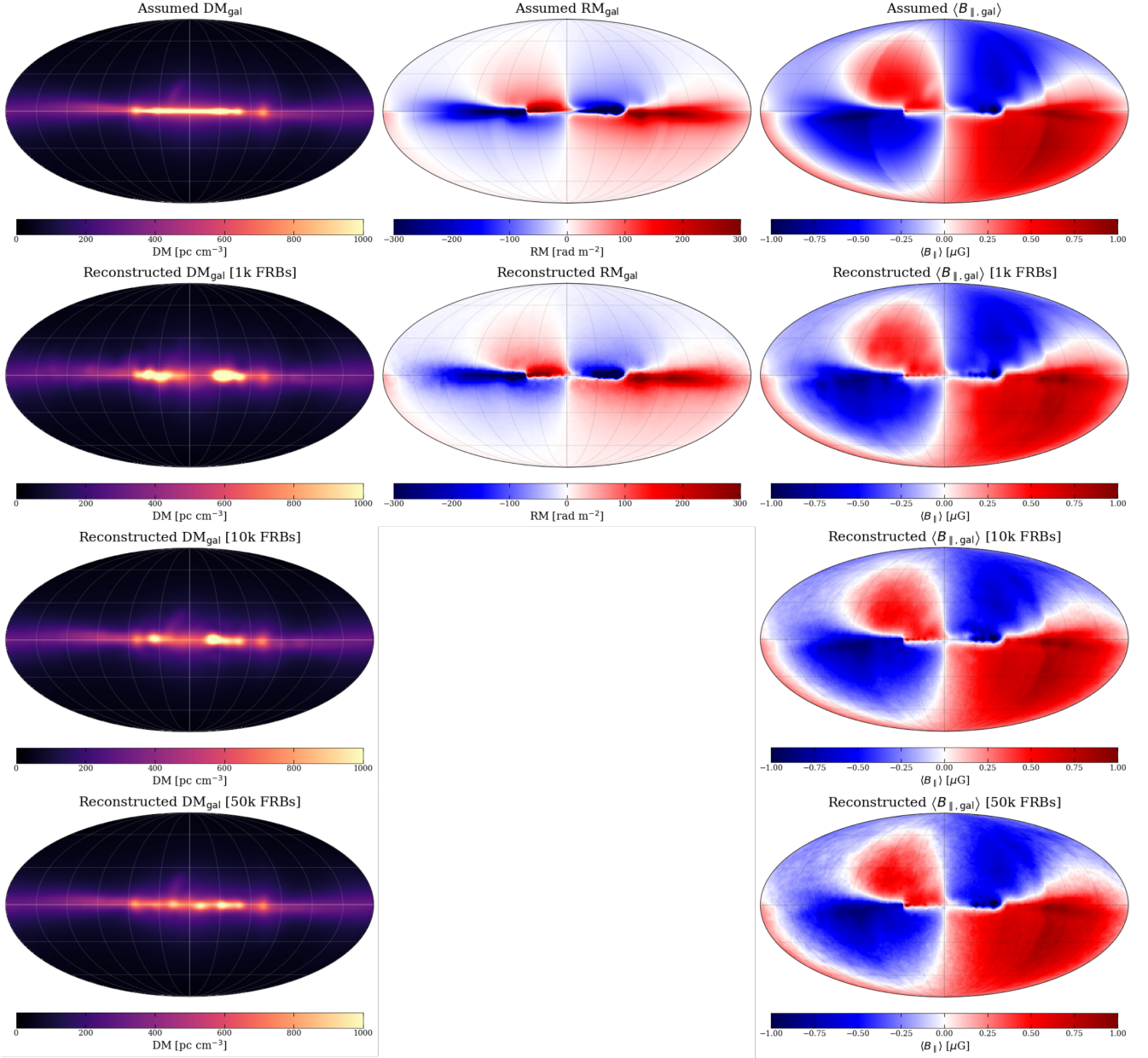


**Figure 4.** Set of reconstructed DM, RM, and  $\langle B_{\parallel} \rangle$  maps in comparison to the expected on-sky observables from *hammurabiX*. All maps are plotted as a Mollweide projection in Galactic coordinates with a resolution of  $\sim 27.5$  arcminutes. The underlying models used for reconstruction explicitly have no extragalactic contributions. The expected total Galactic contribution for each observable is shown in the top row and subsequent rows depict the results of the reconstruction algorithm on progressively larger sets of FRB data (1000, 10000, and 50000). The radio galaxy population has a fixed size and therefore only the RM reconstruction for one run of the joint inference algorithm is presented.

is decreased by  $\sim 150 \text{ pc cm}^{-3}$  and  $|\langle B_{\parallel} \rangle|$  is increased by roughly between  $\sim 0.1$  to  $0.3 \mu\text{G}$  over most of the sky. For a sample of FRBs that are uniformly distributed over the entire sky, as we increase the number of FRBs in the sample, we increase the number of simulated LOS observations per equal-area sub-section of the sky and thus increase the probability of each sub-section containing a nearby, low DM FRB. Therefore, the filter becomes more effective as we increase the number of FRBs in our data set. Hence, this filter is most effective on the sample of 50000 FRBs and becomes progressively less effective for the smaller data sets. For the smallest set (1000 FRBs) we are only able to discard roughly half of the high DM observations without significantly impacting the resolution of the

reconstruction. It should also be noted that this technique discards information pertaining to very small scale Galactic DM structure (i.e. Galactic DM structure with a smaller angular resolution than the equal-area sky patches). In this work, we are focused on large scale structure and this effect does not meaningfully influence our results.

However, this method of constraining the extragalactic DM is not perfect and even after this step, the reconstructed DM ( $\langle B_{\parallel} \rangle$ ) map is still overestimated (underestimated) when contrasted with the expected Galactic contributions from the first row of Figure 4. Namely, there is still a mean extragalactic DM contribution of  $\sim 150 \text{ pc cm}^{-3}$ , which we anticipate from the bottom panel of Figure

2. In Section 5, we attempt to correct for the remaining extragalactic contribution by deriving a possible correction factor as a function of Galactic latitude that is broadly applicable to extragalactic DM observations beyond the simulations employed in this work.

### 4.3 Removing Underlying Model Components

To assess whether the reconstruction results are robust against changes in the underlying model, we redo the analysis in the previous section without including the YT20 halo model in our input model. The first panel of Figure 6 depicts the expected DM contribution from this halo model alone. To generate the map in the second panel, we subtract the reconstruction results without YT20 from those that included both YT20 and YMW16  $n_e$  models. The difference in the subsequent panels of Figure 6 clearly illustrates that the reconstruction is able to identify the change in model, particularly near the GC. Farther out in the halo, the difference map becomes dominated by random pixel-to-pixel variation in the extragalactic component between the two runs. When the extragalactic contribution is minimized in the final panel, we are able to identify the missing halo structure over a broader area of the sky. In this difference map, we encounter lower resolution structure than in the middle panel and this is due to the vastly reduced number of total data points used in the reconstruction (i.e. from 50000 FRBs in the middle panel to 3072 in the bottom panel).

Likewise, we also test whether our algorithm can discern a small change in the GMF model by removing the X-shaped halo component from JF12. Figure 7 depicts the expected  $\langle B_{\parallel} \rangle$  without the X-shaped halo (top), and the reconstructed  $\langle B_{\parallel} \rangle$  before (middle) and after (bottom) applying the DM filter. While removing this feature does not impact the magnitude of  $\langle B_{\parallel} \rangle$  significantly, the large-scale structure, such as the location of reversals in the  $\langle B_{\parallel} \rangle$  direction, is noticeably different from the first row of Figure 4. Hence, we elect to directly compare to the reconstructed maps rather than analyzing difference maps. Again, we see that in both cases (full 50000 FRB sample and the DM-filtered sample), we can identify the change in model and see clear structural differences from the  $\langle B_{\parallel} \rangle$  reconstructions in Figure 5 (which includes the X-shaped halo in the GMF). As expected, the filtered data set more accurately estimates  $\langle B_{\parallel} \rangle$  while the full data set more strongly underestimates  $\langle B_{\parallel} \rangle$ .

## 5 DISCUSSION

### 5.1 Constraining extragalactic DM

As we saw in Section 4, the most prominent impediment in reconstructing Galactic structure in the DM and  $\langle B_{\parallel} \rangle$  sky is the large extragalactic contributions to DM from FRB host galaxies and the IGM. So far, we have applied a filter to remove high DMs in equal-area portions of the sky to help mitigate this problem. Since our simulated lines of sight are roughly uniformly distributed across the sky, applying this filter allows us to effectively extract a subset of FRBs with the lowest total DMs. Physically, this is the equivalent of selecting a subset of the nearest FRBs, distributed in a sphere around the observer. The reconstruction results obtained from using this subset as an input, therefore, provide an upper limit to the total Galactic DM contribution across the sky. However, this upper limit is not ideal as we still cannot isolate the Galactic structure from the remaining extragalactic DM. To tackle this issue in greater detail, we analyze the mean  $\langle B_{\parallel} \rangle$ , observed-to-expected  $\langle B_{\parallel} \rangle$  fraction

and absolute difference from the corresponding `hammurabiX` observable. We break the maps down into latitude strips with a width of 5 deg and sample the entire longitude range at intervals of 30 deg. A full collection of these results is presented in Appendix B for the standard set of assumed input models (YMW16, YT20, and JF12) seen in Figure 5.

Figure 8 shows a visualization of the different DM contributions along a given LOS through our Galaxy and the information provided by using pulsars and FRBs as probes of the Galactic DM. In this section, we aim to derive a correction factor that can be applied to the data to distinguish between Galactic and extragalactic DM contributions. To do this, we model the total observed DM along a given LOS  $DM_{\text{obs}}$  as a latitude dependent term  $DM(b)$ , which encapsulates the Galactic DM contribution, plus a latitude independent term  $DM_0$ , which represents the largely isotropic extragalactic contribution. A number of studies have previously examined the vertical structure of the ISM using DM observations from pulsars (e.g. Gaensler et al. 2008; Ocker et al. 2020) and found that the Galactic DM contribution (which is dominated by the ISM) falls off with latitude as  $1/\sin|b|$ , taking a minimum value towards the Galactic poles. Following this framework, we model  $DM_{\text{obs}}$  as:

$$DM_{\text{obs}} = DM(b) + DM_0 = \frac{DM_{\text{poles}}}{\sin|b|} + DM_0 \text{ pc cm}^{-3}, \quad (12)$$

where  $DM_{\text{poles}}$  is the expected DM contribution from all disk-like Galactic components along the LOS to the Galactic poles. To correct for the extragalactic DM along a given LOS ( $DM_i$ ), we define a correction factor  $F = DM(b)/DM_{\text{obs}}$  such that:

$$F = \frac{DM(b)}{DM(b) + DM_0}; \quad (13)$$

$$DM_{i,\text{corr}} = FDM_i, \quad (14)$$

where  $DM_{i,\text{corr}}$  is the corrected DM along the LOS.

One method of applying this correction factor is to use pulsar data in estimating the value of  $DM_{\text{poles}}$  and then fitting DM data to equation 12 to determine the average value of  $DM_0$  over the sky. Hereafter, this approach will be referred to as the pulsar-based correction. Note that the pulsar-based correction is limited by the most distant pulsar in a data set and cannot probe any additional Galactic DM contributions from the halo beyond that point. When applying this method, we follow the procedure detailed by Ocker et al. (2020), using the same set of pulsar data (see their Table 1), except with DMs computed according to our assumed Galactic  $n_e$  models (YMW16 and YT20). The resulting least squares best fit estimates for equation 12 are  $DM_{\text{poles}} = 33.6 \pm 4.2 \text{ pc cm}^{-3}$  and  $DM_0 = 150.7 \pm 6.3 \text{ pc cm}^{-3}$ . Applying this correction factor to the subset of data that has been filtered to minimize extragalactic DMs then provides a lower limit to the total Galactic DM contribution. Namely, it provides an estimate of the DM contribution from the ISM. With regards to the GMF, applying this correction factor will give us an upper limit for the total Galactic  $|\langle B_{\parallel} \rangle|$ .

Alternatively, we can also use the FRB data itself when computing a correction factor by fitting equation 12 directly to our simulated data that have been filtered to minimize extragalactic DMs, leaving both  $DM_{\text{poles}}$  and  $DM_0$  as free variables. Hereafter, this approach will be referred to as the FRB-based correction. Effectively, the FRB-based correction is directly separating out the DM data into Galactic latitude dependent and independent terms to distinguish Galactic and extragalactic DM contributions. The least squares best fit estimates for the FRB-based correction are  $DM_{\text{poles}} = 41.7 \pm 5.0 \text{ pc cm}^{-3}$  and  $DM_0 = 135.6 \pm 11.1 \text{ pc cm}^{-3}$ .



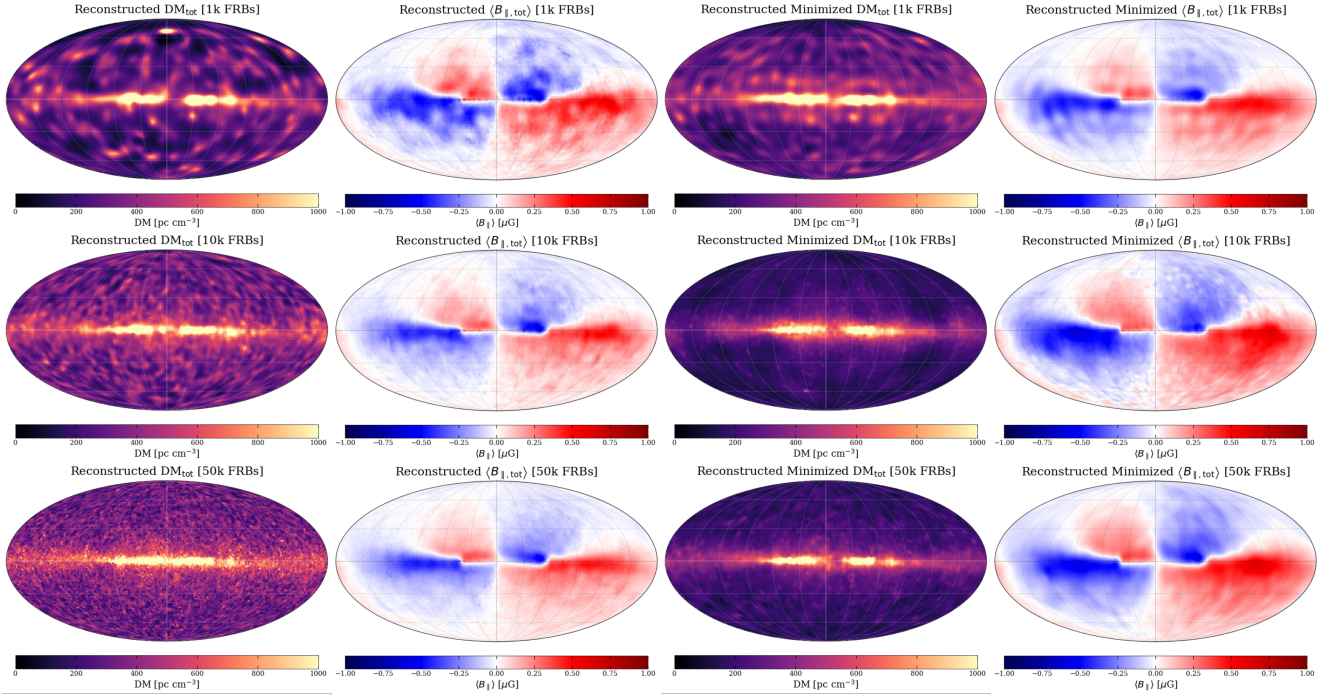


**Figure 5.** As for the first two columns of Figure 4 but now considering the full extent of DM contributions from extragalactic sources as well. The reconstructed RM is the same as Figure 4 and is therefore not plotted here. Again, each subsequent row represents the reconstruction results from successively larger sized data sets. The first two columns are results from the raw (1000, 10000, 50000 FRB) data sets and the last two columns are after they have been filtered to minimize the extragalactic DM contributions.

Since FRBs are extragalactic sources and probe the entirety of the MW, the FRB-based correction is able to better estimate the Galactic contributions from the MW halo than the pulsar-based correction. However, we expect the furthest reaches of the MW halo to be an extended spherical  $n_e$  halo (Yamasaki & Totani 2020), which will add a roughly constant and isotropic DM contribution across the sky, and be indistinguishable from the extragalactic contributions. Therefore, while the FRB-based correction provides a better estimate of the total Galactic DM contribution than the pulsar-based estimate, it is still does not exactly reconstruct the input Galactic DM and  $\langle B_{||} \rangle$ .

In both the pulsar-based and FRB-based corrections, we note that the  $1/\sin|b|$  assumption from equation 12 breaks down as  $b \rightarrow 0$ . As a result, our correction factor becomes unreliable at very low Galactic latitudes and, subsequently, we only apply corrections for  $|b| > 10$  deg. Figure 9 summarizes the various steps taken to disentangle the Galactic and extragalactic DM contributions and shows that the FRB-based correction provides the better estimate of the input Galactic DM at  $|b| > 10$  deg. Specifically, the combination of applying a filter to remove high DMs in equal-area portions of the sky and then applying the FRB-based correction (via equations 12, 13, and 14) reduces the reconstructed DM by an average of  $272.9 \pm 8.4 \text{ pc cm}^{-3}$  for  $|b| > 10$  deg and the absolute difference between this corrected DM and the input model DM is on average  $\lesssim 6.1 \pm 2.4 \text{ pc cm}^{-3}$  for  $|b| > 10$  deg. Applying the reciprocal of equation 13 to  $\langle B_{||} \rangle$  improves the accuracy of our magnetic field reconstruction as well. Figure 10 depicts the results of applying our pulsar-based and FRB-based corrections to the observed  $\langle B_{||} \rangle$  at slices taken at intervals of 30 deg in Galactic longitude. For each of the panels in Figure 10, the absolute difference between the FRB-based correction of  $\langle B_{||} \rangle$  and input model  $\langle B_{||} \rangle$  is on average  $\lesssim 0.06 \pm 0.04 \text{ } \mu\text{G}$  for  $|b| > 10$  deg.

To further establish that the correction factor can be applied beyond the standard assumed model examined above, we repeat the same process after removing the X-shaped halo from the GMF model. Applying the same corrections, we are again able to recover DM and  $\langle B_{||} \rangle$  structure that better resembles the expected Galactic observables. In this case, following the pulsar-based correction gives us a best fit of  $\text{DM}_{\text{poles}} = 33.6 \pm 4.2 \text{ pc cm}^{-3}$  and  $\text{DM}_0 = 152.0 \pm 6.3 \text{ pc cm}^{-3}$ , and following the FRB-based correction gives  $\text{DM}_{\text{poles}} = 42.3 \pm 4.9 \text{ pc cm}^{-3}$  and  $\text{DM}_0 = 135.8 \pm 10.9 \text{ pc cm}^{-3}$ . Taking the absolute difference between our best correction (FRB-based) and the input DM ( $\langle B_{||} \rangle$ ), we find that on average they differ by  $\lesssim 4.8 \pm 1.8 \text{ pc cm}^{-3}$  ( $\lesssim 0.07 \pm 0.06 \text{ } \mu\text{G}$ ) for  $|b| > 10$  deg. See Appendix B for the full set of corresponding plots.

## 5.2 Application to Observed Data & Caveats

Throughout this paper, we have presented results based on a simplified model. Here, we discuss application this work has to current and future FRB observations. Firstly, these simulated observations are derived from models of various components of the MW. While these models are useful for describing the Galactic structure on large scales, we expect there to be a great deal more turbulence and small scale structure in observations (e.g. compare the modelled  $\text{RM}_{\text{gal}}$  from Figure 4 to the results presented by Oppermann et al. 2012 and Hutschenreuter & Enßlin 2020, which are derived from observations). This has implications on the expected power spectra for both the RM and DM skies. In this work, our inference algorithm has expected rather steep power spectra, corresponding to sky maps dominated by large structures such as the Galactic disc. For a real data application, this expectation (i.e. the prior on the power spectrum slope) would have to be adapted.



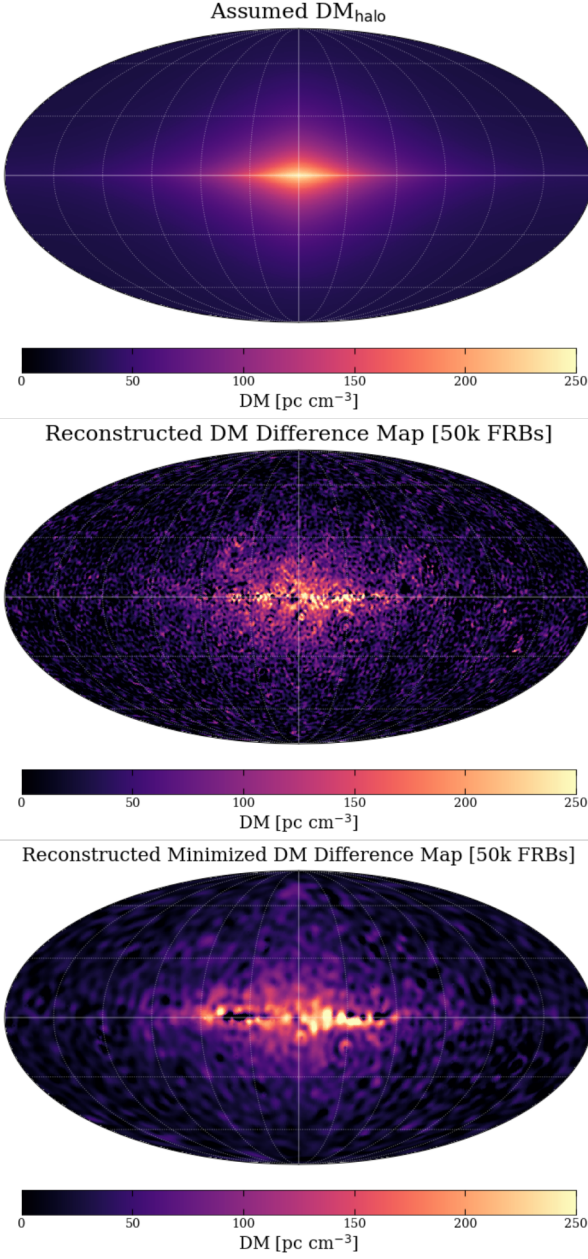


**Figure 6.** (Top) DM contribution from the halo component of our  $n_e$  model (YT20) generated from *hammurabiX*. (Middle) Difference map created by subtracting the reconstructed DM map without the YT20 halo contribution from the reconstructed result when assuming both YMW16 and YT20 models. This map uses the largest FRB population (50000 FRBs). (Bottom) Same as the middle plot but after applying the filter to minimize extragalactic DM contributions (3072 FRBs).

The simulated FRB populations used in this work are also largely simplified versions of observed FRBs. For instance, in the first CHIME/FRB catalogue (CHIME/FRB Collaboration et al. 2021), the observed sky distribution of sources only extends down to  $\text{DEC} \sim -11$  deg and is not uniformly distributed. This is due to the transiting observing mode used for CHIME; the distribution of FRBs detected is most dense around the celestial north pole and decreases away from it. This is a major point to note because, in our simulated observations, we had a fairly evenly distributed FRB population over the whole sky which allowed for the joint inference

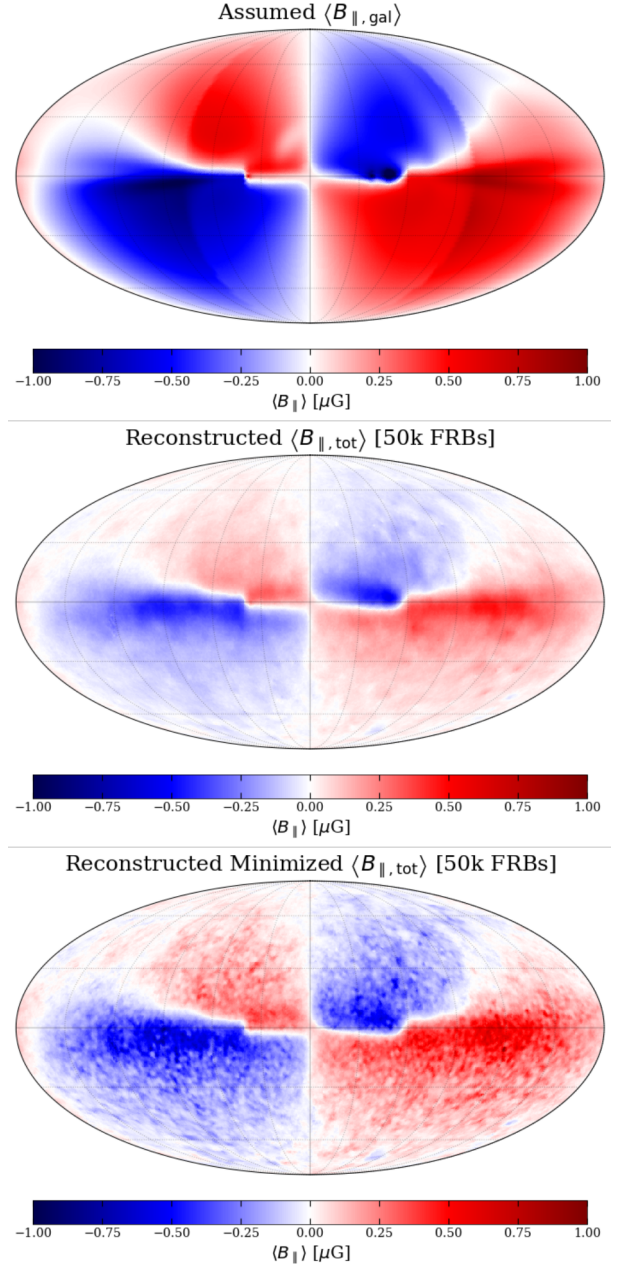


**Figure 7.** (Top) Expected  $\langle B_{\parallel} \rangle$  from *hammurabiX* when excluding the poloidal X-shaped halo from the JF12 model. Reconstructed  $\langle B_{\parallel} \rangle$  maps with 50000 simulated FRBs (middle) and the 3072 DM-filtered data points (bottom) are also plotted.

to parameterize structure even with only 1000 FRBs. In reality, we may require many more observations to achieve a sufficient minimum source density over the entire observable sky area. However, it should be noted that DM observations from several FRB surveys can be combined into a single catalogue and input into the joint inference algorithm (similar to RM catalogue utilized in this work).

We note that while the extragalactic DM contribution in our model is isotropic (which we expect observationally on large scales), in reality it may be structured over small scales. This would be due to contributions from intervening extragalactic sources along the LOS (e.g. M31, the Magellanic Clouds, and LGM) (e.g. Prochaska & Zheng 2019), which is not entirely deleterious as it allows for

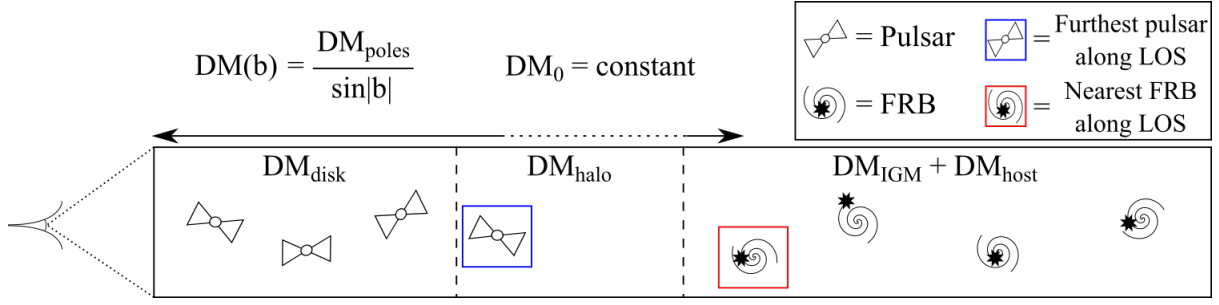


**Figure 8.** A simple illustration depicting the various components of DM contributions along a given LOS through the MW, as probed by pulsars and FRBs. The observed DM is comprised of contributions from the MW disk ( $DM_{\text{disk}}$ ), MW halo ( $DM_{\text{halo}}$ ), IGM ( $DM_{\text{IGM}}$ ), and the FRB host galaxy ( $DM_{\text{host}}$ ). Pulsars are depicted as circles with two symmetrical cones and FRBs and their host galaxies are represented by black bursts within a spiral; the farthest pulsar and nearest FRB are highlighted as they provide a lower and upper limit on the total Galactic DM along the LOS, respectively. Dashed lines are used to show the boundary between the MW disk, halo, and the IGM and arrows are used to indicate the physical regions for which our model (equation 12) is estimating DM contributions. The pulsar-based correction models everything beyond the furthest pulsar as a Galactic latitude independent extragalactic DM contribution, while the FRB-based correction includes more of the halo in the latitude dependent Galactic DM contribution. Not all of the Galactic halo is included in the latitude dependent term, even by the FRB-based correction, and the dotted section of the arrows signifies the ambiguity regarding the exact extent to which the halo is classified as Galactic DM contribution. Note that most pulsars are located within the MW disk but there are some located in the MW halo, similar to the example depicted in this diagram.

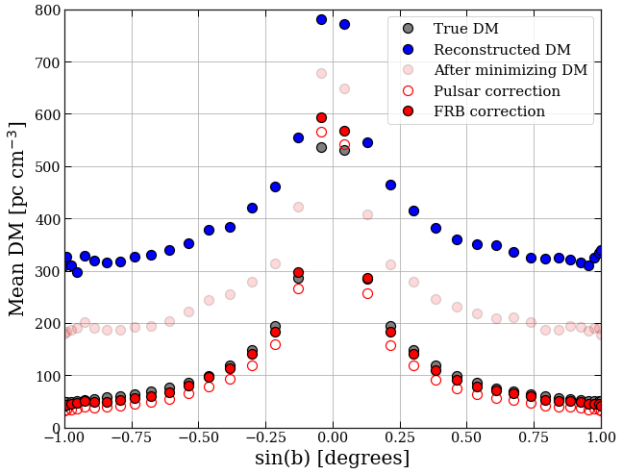


**Figure 9.** Mean DM over  $0 \text{ deg} < \ell < 360 \text{ deg}$  plotted as a function of the sine of the Galactic latitude  $b$ . The input Galactic DM contributions from *hammurabiX* are plotted in grey. Blue points represent the full set of 50000 simulated FRB observations and evidently contain significant extragalactic contributions. Filtering the data to remove high DM lines of sight, as mentioned in Section 4, reduces the extragalactic contribution and provides an upper limit to the Galactic DM; these points are plotted as light red. Further, applying the pulsar-based DM correction estimates the  $DM_{\text{IGM}}$  and places a lower limit on the total Galactic DM—as depicted by the hollow red points. Instead, applying the FRB-based correction by allowing both  $DM_{\text{poles}}$  and  $DM_{\text{xgal,mean}}$  to be free parameters, produces a much closer fit to the input Galactic DM and is plotted in dark red. Note that the corrections applied to obtain the hollow red and dark red points are only valid for  $|b| > 10 \text{ deg}$  (i.e.  $|\sin(b)| \gtrsim 0.17$ ).

the study of DM structure inherent to these objects (e.g. Connor & Ravi 2021). However, for the purposes of studying the MW, these contributions will require a more careful handling of the data or the inference model to constrain.

Another consideration is that the current CHIME/FRB catalogue has relatively low positional accuracy, with positional uncertainties up to  $\sim 0.5 \text{ deg}$ . These positional uncertainties give us a lower limit on the size of Galactic structure that can be resolved using our joint-inference reconstruction method. However, the mean

spacing of our FRBs is larger than the typical FRB positional uncertainties after applying the DM filtering criterion, and thus the former dominates the scale of resolvable Galactic structures. Nonetheless, to ensure that these uncertainties do not significantly affect the joint-inference reconstruction, we repeated our analysis (Section 4) after shifting each of the simulated FRBs in our sample by a randomly drawn RA and DEC uncertainty from the CHIME/FRB catalogue. The typical on-sky offset of each simulated FRB from its original position was  $\sim 0.26 \text{ deg}$ . After applying the DM filtering criterion and generating the reconstructed map using the shifted data set, the average percent difference in DM for a given pixel was  $\sim 4 - 5\%$  compared to the original reconstruction. The maximum percent difference in DM for a given pixel was  $\sim 40\%$ . Further, the estimates for  $DM_{\text{poles}}$  and  $DM_0$  from the reconstruction using shifted FRBs only varied  $\sim 2 - 3\%$  from the original values ( $DM_{\text{poles}} = 41.7 \pm 5.0 \text{ pc cm}^{-3}$  and  $DM_0 = 135.6 \pm 11.1 \text{ pc cm}^{-3}$ ) and were in agreement with the quoted uncertainties. Therefore, we find that artificially including FRB positional uncertainties typical of the CHIME/FRB Collaboration et al. (2021) catalogue does not significantly change the reconstruction results and major conclusions of our analysis. We also note that we will have better FRB localizations with future FRB surveys, which are described in further detail below, and therefore we expect the typical positional accuracy of FRBs to improve in the near future.

As the existing catalog of FRBs grows, the aspects of future FRB observations that will be particularly valuable to developing this reconstruction method include: (i) a large number of nearby FRBs (since low DM FRBs are more informative to this method than distant, high DM FRBs), (ii) all-sky coverage, and (iii) associated redshift information (allowing us to estimate extragalactic DM contributions). The premier survey to obtain such a data set currently, and in the near future, is CHIME/FRB with its outtrigger facilities which will supplement the high detection rate and daily all-hemisphere coverage of CHIME/FRB with better on-sky localization, thus leading to more associated redshift estimates (for details regarding the CHIME outtrigger systems and localization of FRBs through Very Long Baseline Interferometry, see Mena-Parra et al. 2022; Cassanelli et al. 2022). On longer time scales, we expect the Hydrogen Intensity and Real-time Analysis Experiment (HIRAX, Newburgh et al. 2016) and the Canadian Hydrogen Ob-

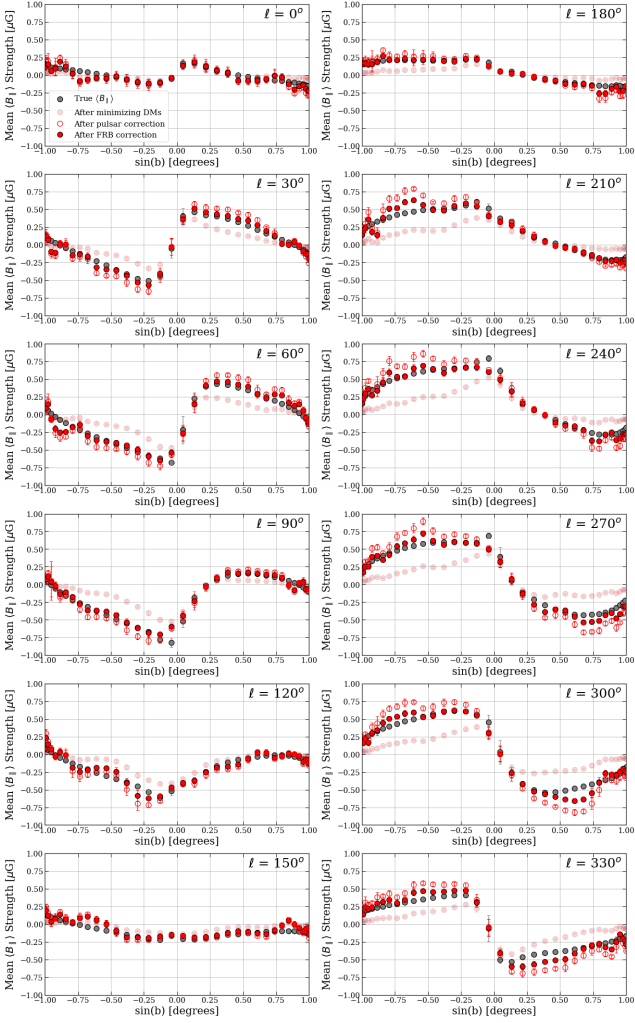


**Figure 10.** A comprehensive look at the effects of applying the pulsar-based and FRB-based DM corrections, shown in Figure 9 to  $\langle B_{\parallel} \rangle$  at various longitudes cut. Each sub-plot is offset by 30 deg in Galactic longitude  $\ell$  and marker selection is identical to Figure 9—with light red (hollow red) points now representing a lower limit (upper limit) in  $\langle B_{\parallel} \rangle$ .

servatory and Radio-transient Detector (CHORD, Vanderlinde et al. 2019) to come online and have similar, or higher, FRB rates than CHIME/FRB. However, HIRAX and CHORD will have a much smaller daily sky coverage than CHIME/FRB and require manual repointing, so the timescale or capacity for  $\geq \pi$ sr deg sky coverage by either survey alone is uncertain. The Deep Synoptic Array-2000 (DSA-2000) is expected to see first light in 2026, covering  $\sim 3\pi$ sr deg every few months and detecting/localizing FRBs at a rate of  $\sim 10^4 \text{ year}^{-1}$  (Hallinan et al. 2019). In addition, the new coherent search system on the Commensal Real-Time Australia Square Kilometer Array Pathfinder Fast-Transient survey (CRAFT, Macquart et al. 2010) is expected to provide  $\sim 1.5$  localized FRBs per day. CRAFT is a commensal search with the Australian Square Kilometre Array Pathfinder (ASKAP, Hotan et al. 2021) survey science projects (Johnston et al. 2008) and will cover the entire southern sky in approximately 5 years. With the reconstruction technique described in Section 3, we can input a combined FRB catalogue comprising data from multiple surveys, allowing us to exploit the complementary sky coverage of different surveys (e.g.

CHIME/FRB, CHORD, and the DSA-2000 in the northern hemisphere, and HIRAX and CRAFT in the southern hemisphere).

While we expect the catalog of FRBs to increase greatly in the near future, the number of radio galaxy RMs will proliferate as we get data releases from large sky radio surveys such as VLASS and POSSUM. In the next 5 years, the radio galaxy RM catalog will increase from  $\sim 50000$  to  $\sim 10^6$  sources (Heald et al. 2020). Therefore, as is currently the case (see Section 1), the number of radio galaxy RMs will still far exceed the number of FRB RMs in the near future.

### 5.3 Interpreting GMF Results & Exceptions

Throughout this study we have been focused on  $\langle B_{\parallel} \rangle$ ; it is important to contextualize what exactly  $\langle B_{\parallel} \rangle$  describes relative to  $B_{\parallel}$  or the full GMF and to remember the assumptions that went into deriving equation 4 and the resulting reconstructions.  $\langle B_{\parallel} \rangle$  provides the electron density weighted average magnetic field strength and net direction—this quantity is not necessarily equivalent to  $B_{\parallel}$  and only provides the averaged  $B_{\parallel}$  strength and net orientation along the entire distance between the observer and the emitting object. Hence,  $\langle B_{\parallel} \rangle$  measurements do not provide us with knowledge of  $B_{\parallel}$  at any specific distance along the LOS. A reconstruction of the  $\langle B_{\parallel} \rangle$  sky also does not provide us with full information about the GMF. To get a more complete picture of the GMF,  $\langle B_{\parallel} \rangle$  must be analyzed alongside the plane-of-sky magnetic field  $B_{\perp}$ .

Recall that, for equation 4, we made the implicit assumption that the electron density  $n_e$  and  $B_{\parallel}$  are uncorrelated—however this may not always be a good assumption. Previous studies (e.g. Beck et al. 2003; Seta & Federrath 2021) have shown that measurements of  $\langle B_{\parallel} \rangle$  using equation 4 may be underestimated or overestimated in regions where  $n_e$  and  $B_{\parallel}$  are negatively or positively correlated, respectively. Specifically, Seta & Federrath (2021) showed that  $n_e$  and  $B_{\parallel}$  are largely uncorrelated over kpc scales but may break down at sub-kpc scales. Since this work is primarily focused on reconstructing  $\langle B_{\parallel} \rangle$  over large Galactic scales, equation 4 provides a valid estimate of the true underlying  $B_{\parallel}$ .

This study focuses on the halo rather than the disk. The halo structure is likely much smoother than the disk since in the disk we expect to find more dense patches of electrons, e.g., due to star formation regions. We expect that equation 4 is more likely to be true in a region such as the halo, where the electron density is smoothly varying.

## 6 CONCLUSIONS

We present a new method of reconstructing all-sky  $\langle B_{\parallel} \rangle$  information for the Galactic magnetic field (GMF) using a rotation measure–dispersion measure (RM–DM) joint inference algorithm based on information field theory (Enßlin et al. 2009; Enßlin 2019) and demonstrate its effectiveness on simulated line of sight (LOS) observations to radio galaxies and fast radio burst (FRB) populations. The joint inference is able to constrain DM, RM, and  $\langle B_{\parallel} \rangle$  along a given LOS by exploiting correlations of nearby data points and each sky map is parameterized as a non-linear combination of Gaussian sky maps, assuming  $\text{RM}_{\text{gal}}$  and  $\text{DM}_{\text{gal}}$  are modelled by equations 10 and 11, respectively.

Given only Galactic inputs, which serve as a baseline test but are otherwise unphysical, both the large and small scale Galactic structure of the reconstruction result is qualitatively well-matched



with the input model (Figure 4). While the reconstruction is hindered with the presence of extragalactic DM contributions, we detail a method of reducing and characterizing this component of DM observations (Figure 9) by: (i) systematically filtering out high DM observations in equal-area subsections of the sky, which provides an upper limit on Galactic DM and (ii) applying either a pulsar-based or FRB-based DM correction factor for  $|b| > 10$  deg (equations 12, 13, and 14) for an estimate of the total Galactic DM contribution.

In general, the reconstruction performs noticeably better on a larger sample of simulated FRBs (50000 FRBs) but is still able to replicate some large-scale structures, such as the high DM and  $\langle B_{\parallel} \rangle$  magnitude in the Galactic plane, even with only 1000 FRBs. The reconstruction is also able to identify deviations in the underlying models for both the  $n_e$  distribution (removal of the Yamasaki & Totani 2020 halo model, see Figure 6) and GMF (removal of the Jansson & Farrar 2012 X-shaped halo, see Figure 7).

The results are supplemented with a discussion of the differences between our simulations and FRB observations which informs the feasibility of using current and future FRB data as a probe for large scale Galactic structure. Chief among the challenges of applying this method to FRB observations is the low number of data points that are currently publicly available and that they are not uniformly distributed over the sky. However, the rapid rate at which FRBs are being observed, especially by CHIME/FRB, is a promising step towards overcoming this hurdle. Overall, this work provides a powerful tool for studying DM, RM, and  $\langle B_{\parallel} \rangle$  across the entire sky with the rapidly growing FRB catalogue. In addition, there are still various avenues for further study based on this work, including:

- (i) Incorporating extragalactic contributions, particularly for DM, directly into the joint inference algorithm as effective noise (similar to the approach presented by Oppermann et al. 2015; Hutschenreuter & Enßlin 2020);
- (ii) Incorporating Galactic pulsar DM and RM measurements or Emission measures;
- (iii) Incorporating FRB positional uncertainties directly into the reconstruction by resampling positions in the Numerical Information Field Theory Python package (NIFTy);
- (iv) Designing a simulated data set that more closely resembles the sky-coverage and sensitivity of CHIME/FRB to estimate the number of FRB observations required to perform an accurate reconstruction;
- (v) Testing the joint inference algorithm and correction factor (equation 13) assuming other GMF or  $n_e$  models. This may also include the injection of a random component to these models;
- (vi) Applying this method directly to FRB observations to study all-sky  $\langle B_{\parallel} \rangle$  and constrain the GMF structure on an unprecedented scale. This could further incorporate  $B_{\perp}$  information derived from dust polarization (e.g. Planck Collaboration et al. 2016c) to analyze the 3D GMF.

## 7 ACKNOWLEDGEMENTS

We thank Tess Jaffe and Jiaxin Wang for sharing information regarding *hammurabiX* and Ziggy Pleunis, Samantha Berek, and Steffani Grondin for useful comments on the manuscript. We also thank the anonymous reviewer for careful reading of the manuscript and for providing constructive feedback. The Dunlap Institute is funded through an endowment established by the David Dunlap family and the University of Toronto. SH acknowledges funding from the European Research Council (ERC) under the European Union’s Horizon 2020 research and innovation programme (grant agreement No.

772663). JLW and BMG acknowledge the support of the Natural Sciences and Engineering Research Council of Canada (NSERC) through grant RGPIN-2015-05948, and of the Canada Research Chairs program.

## 8 DATA AVAILABILITY

No new data were generated or analysed in support of this research. Detailed steps on how to recreate the simulated observations are laid out in section 2.

## REFERENCES

- Arras P., et al., 2019, *Astrophysics Source Code Library*, p. ascl:1903.008
- Arras P., Frank P., Haim P., Knollmüller J., Leike R., Reinecke M., Enßlin T., 2022, *Nature Astronomy*,
- Bannister K. W., et al., 2019, *Science*, 365, 565
- Beck R., 2009, *Ap&SS*, 320, 77
- Beck R., Shukurov A., Sokoloff D., Wielebinski R., 2003, *A&A*, 411, 99
- CHIME/FRB Collaboration et al., 2018, *ApJ*, 863, 48
- CHIME/FRB Collaboration et al., 2020, *Nature*, 587, 54
- CHIME/FRB Collaboration et al., 2021, *ApJS*, 257, 59
- Cassanelli T., et al., 2022, *AJ*, 163, 65
- Chatterjee S., et al., 2017, *Nature*, 541, 58
- Connor L., Ravi V., 2021, arXiv e-prints, p. arXiv:2107.13692
- Cordes J. M., Chatterjee S., 2019, *ARA&A*, 57, 417
- Cordes J. M., Lazio T. J. W., 2002, arXiv e-prints, pp astro-ph/0207156
- Enßlin T. A., 2019, *Annalen der Physik*, 531, 1800127
- Enßlin T. A., Frommert M., Kitaura F. S., 2009, *Phys. Rev. D*, 80, 105005
- Ferrière K. M., 2001, *Reviews of Modern Physics*, 73, 1031
- Ferrière K., West J. L., Jaffe T. R., 2021, *MNRAS*, 507, 4968
- Gaensler B. M., Madsen G. J., Chatterjee S., Mao S. A., 2008, *Publ. Astron. Soc. Australia*, 25, 184
- Gardner D. W., van Leeuwen J., Connor L., Petroff E., 2019, *A&A*, 632, A125
- Górski K. M., Hivon E., Banday A. J., Wandelt B. D., Hansen F. K., Reinecke M., Bartelmann M., 2005, *ApJ*, 622, 759
- Hales C. A., Max-Moerbeck W., Roshi D. A., Rupen M. P., 2016, *ApJ*, 823, 93
- Hallinan G., et al., 2019, in *Bulletin of the American Astronomical Society*, p. 255 (arXiv:1907.07648)
- Han J. L., Manchester R. N., Qiao G. J., 1999, *MNRAS*, 306, 371
- Haverkorn M., 2015, in *Magnetic Fields in Diffuse Media*, p. 483, doi:10.1007/978-3-662-44625-6\_17
- Heald G., et al., 2020, *Galaxies*, 8, 53
- Hotan A. W., et al., 2021, *Publ. Astron. Soc. Australia*, 38, e009
- Hutschenreuter S., Enßlin T. A., 2020, *A&A*, 633, A150
- Hutschenreuter S., et al., 2022, *A&A*, 657, A43
- Jaffe T. R., 2019, *Galaxies*, 7, 52
- Jaffe T. R., et al., 2013, *MNRAS*, 431, 683
- Jansson R., Farrar G. R., 2012, *ApJ*, 757, 14
- Johnston-Hollitt M., et al., 2015, in *Advancing Astrophysics with the Square Kilometre Array*, SKA Organization, p. 92 (arXiv:1506.00808)
- Johnston S., et al., 2008, *Experimental Astronomy*, 22, 151
- Keane E., et al., 2015, in *Advancing Astrophysics with the Square Kilometre Array*, SKA Organization, p. 40 (arXiv:1501.00056)
- Knollmüller J., Enßlin T. A., 2019, arXiv e-prints, p. arXiv:1901.11033
- Krause M., 2009, in *Revista Mexicana de Astronomía y Astrofísica Conference Series*, pp 25–29 (arXiv:0806.2060)
- Krause M., et al., 2020, *A&A*, 639, A112
- Lawrence E., Vander Wiel S., Law C., Burke Spolaor S., Bower G. C., 2017, *AJ*, 154, 117
- Lorimer D. R., Bailes M., McLaughlin M. A., Narkevic D. J., Crawford F., 2007, *Science*, 318, 777
- Macquart J.-P., et al., 2010, *Publ. Astron. Soc. Australia*, 27, 272



- Macquart J. P., et al., 2020, *Nature*, **581**, 391
- Manchester R. N., 1972, *ApJ*, **172**, 43
- Manchester R. N., 1974, *ApJ*, **188**, 637
- Manchester R. N., Hobbs G. B., Teoh A., Hobbs M., 2005, VizieR Online Data Catalog, p. VII/245
- Marcote B., et al., 2020, *Nature*, **577**, 190
- Mckinven R., et al., 2021, *ApJ*, **920**, 138
- Mena-Parra J., et al., 2022, *AJ*, **163**, 48
- Newburgh L. B., et al., 2016, in Hall H. J., Gilmozzi R., Marshall H. K., eds, Society of Photo-Optical Instrumentation Engineers (SPIE) Conference Series Vol. 9906, Ground-based and Airborne Telescopes VI. p. 99065X ([arXiv:1607.02059](https://arxiv.org/abs/1607.02059)), doi:10.1117/12.2234286
- Ng C., et al., 2020, *MNRAS*, **496**, 2836
- Noutsos A., Johnston S., Kramer M., Karastergiou A., 2008, *MNRAS*, **386**, 1881
- Ocker S. K., Cordes J. M., Chatterjee S., 2020, *ApJ*, **897**, 124
- Oppermann N., et al., 2012, *A&A*, **542**, A93
- Oppermann N., et al., 2015, *A&A*, **575**, A118
- Planck Collaboration et al., 2016a, *A&A*, **594**, A10
- Planck Collaboration et al., 2016b, *A&A*, **594**, A13
- Planck Collaboration et al., 2016c, *A&A*, **596**, A103
- Platts E., Weltman A., Walters A., Tendulkar S. P., Gordin J. E. B., Kandhai S., 2019, *Phys. Rep.*, **821**, 1
- Prochaska J. X., Zheng Y., 2019, *MNRAS*, **485**, 648
- Rand R. J., Lyne A. G., 1994, *MNRAS*, **268**, 497
- Rane A., Lorimer D. R., Bates S. D., McMan N., McLaughlin M. A., Rajwade K., 2016, *MNRAS*, **455**, 2207
- Ravi V., et al., 2019, *Nature*, **572**, 352
- Schnitzeler D. H. F. M., 2010, *MNRAS*, **409**, L99
- Seta A., Federrath C., 2021, *MNRAS*, **502**, 2220
- Sobey C., et al., 2019, *MNRAS*, **484**, 3646
- Sun X.-H., Reich W., 2010, *Research in Astronomy and Astrophysics*, **10**, 1287
- Terral P., Ferrière K., 2017, *A&A*, **600**, A29
- Thornton D., et al., 2013, *Science*, **341**, 53
- Vanderlinde K., et al., 2019, in Canadian Long Range Plan for Astronomy and Astrophysics White Papers. p. 28 ([arXiv:1911.01777](https://arxiv.org/abs/1911.01777)), doi:10.5281/zenodo.3765414
- Waelkens A., Jaffe T., Reinecke M., Kitaura F. S., Enßlin T. A., 2009, *A&A*, **495**, 697
- Wang J., Jaffe T. R., Enßlin T. A., Ullio P., Ghosh S., Santos L., 2020, *ApJS*, **247**, 18
- Yamasaki S., Totani T., 2020, *ApJ*, **888**, 105
- Yao J. M., Manchester R. N., Wang N., 2017, *ApJ*, **835**, 29

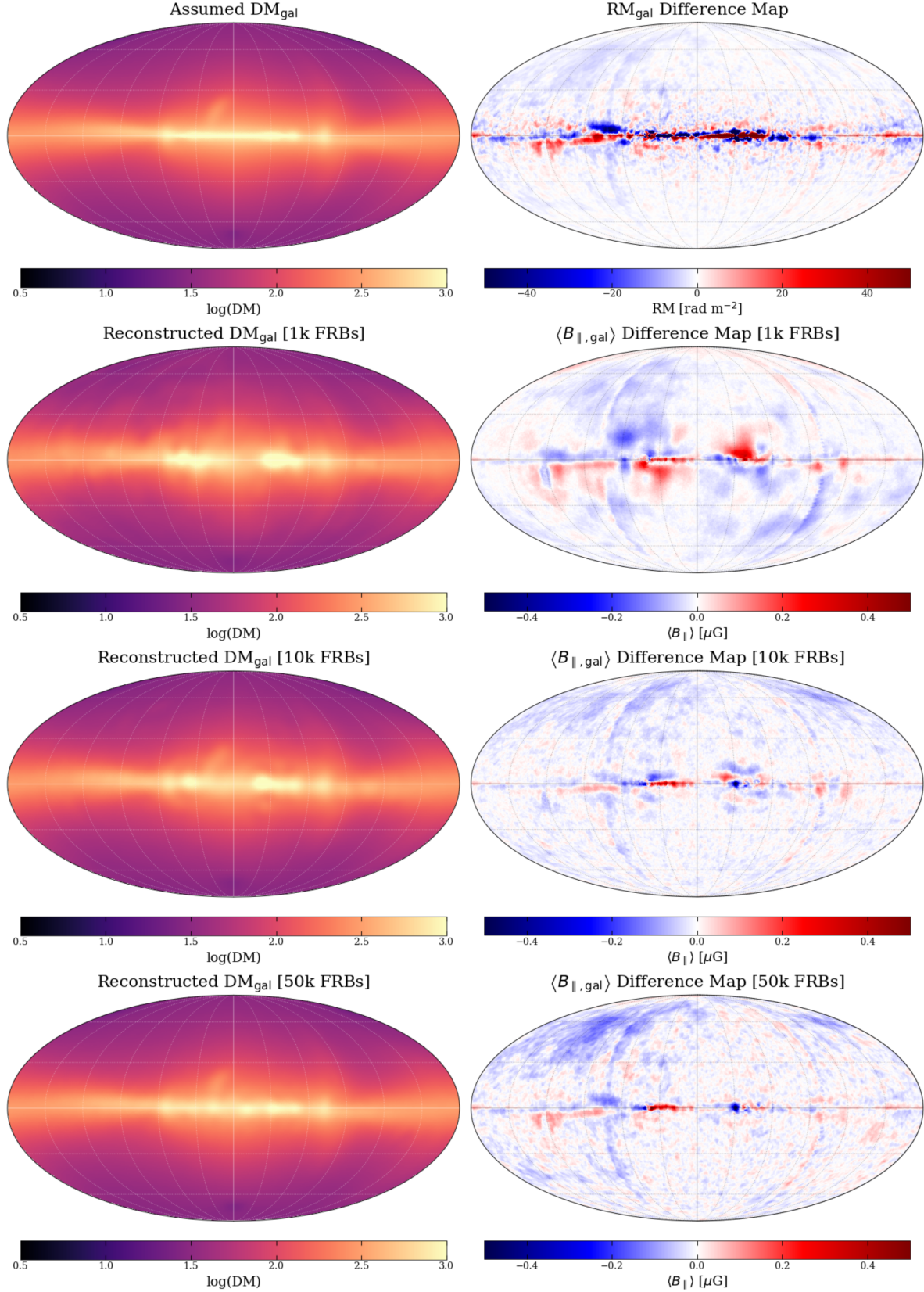
## APPENDIX A: SUMMARY OF RECONSTRUCTION RESULTS

Figure A1 presents the results from Figure 4 in alternative ways to better visualize the differences between the reconstruction results and underlying fields. The left hand column shows the same DM maps from Figure 4 but in a log base 10 scale to better see low-DM regions away from the Galactic plane. The right hand column shows difference maps between the reconstructed RM and  $\langle B_{\parallel} \rangle$  in Figure 4 and the corresponding *hammurabiX* outputs. Summarized in Figures A2, A3, and A4 are the full set of reconstructed maps with corresponding error maps. The setup of the results is identical in all three plots, starting with the largest data set of 50000 FRBs in the first row and showing the results from smaller data sets in consecutive rows. Figure A2 also has an additional row for the reconstructed RM results, which is not present in the other plots. In the case of Figure A4, recall that the data sets are much smaller after being filtered in DM space (3072, 768, and 563 FRBs respectively) but are labelled with regard to the initial size of the data set prior to the data reduction step.

## APPENDIX B: CORRECTION FACTOR ANALYSIS

Figures B1 and B2 illustrate the offset between the expected  $\langle B_{\parallel} \rangle$  (grey points) and the reconstruction results (blue points for the full data set and red points for the DM filtered set), which primarily arises due to extragalactic DM contributions. Figures B1 considers the standard model (YMW16, YT20, JF12) used throughout the paper, while Figure B2 shows reconstructions after removing the X-shaped halo from JF12. Three sub-plots are produced for each slice centered at 30 deg intervals in Galactic longitude: (i) the first shows the mean  $\langle B_{\parallel} \rangle$  as a function of Galactic latitude; (ii) the second presents the observed-to-expected  $\langle B_{\parallel} \rangle$  ratio, with a dashed line representing where the ratio is unity; (iii) the third plots the absolute difference between the reconstruction results and the expected  $\langle B_{\parallel} \rangle$ .

Figures B3 and B4 are similar to Figures 9 and 10 in Section 5 except after the removal of the X-shaped halo from the JF12 model. Again the same set of DM corrections in Section 5.1 (derived from equations 12–14) are applied to better recover Galactic structure.



**Figure A1.** Supplementary Figure to Figure 4 presenting DM sky maps in log-space to better visualize low-DM regions away from the Galactic plane. Difference maps comparing RM and  $\langle B_{\parallel} \rangle$  reconstruction results to the corresponding `hammurabiX` maps, seen in Figure 4, are also presented in the right hand column to better highlight the small differences between the reconstruction and underlying fields.

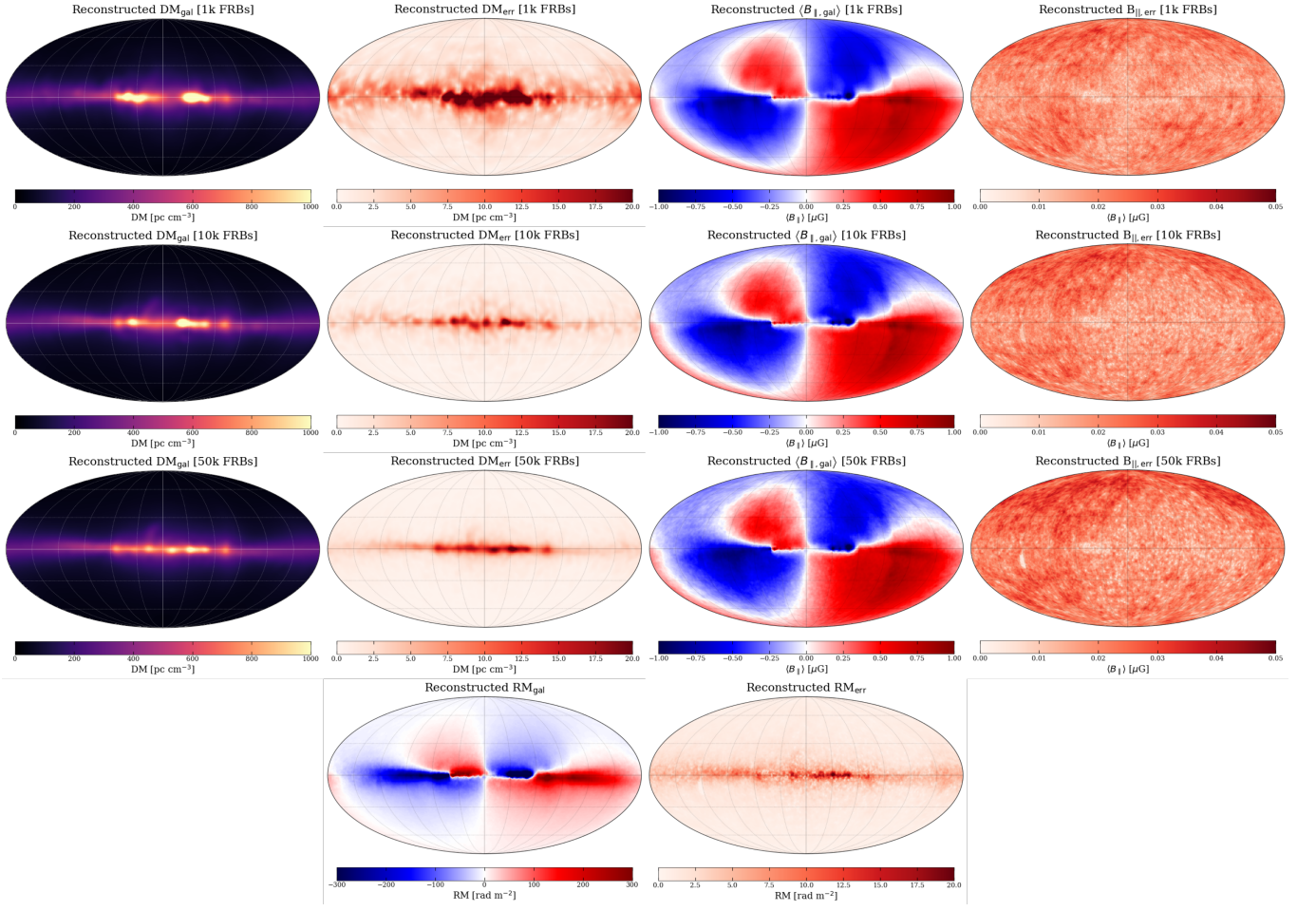
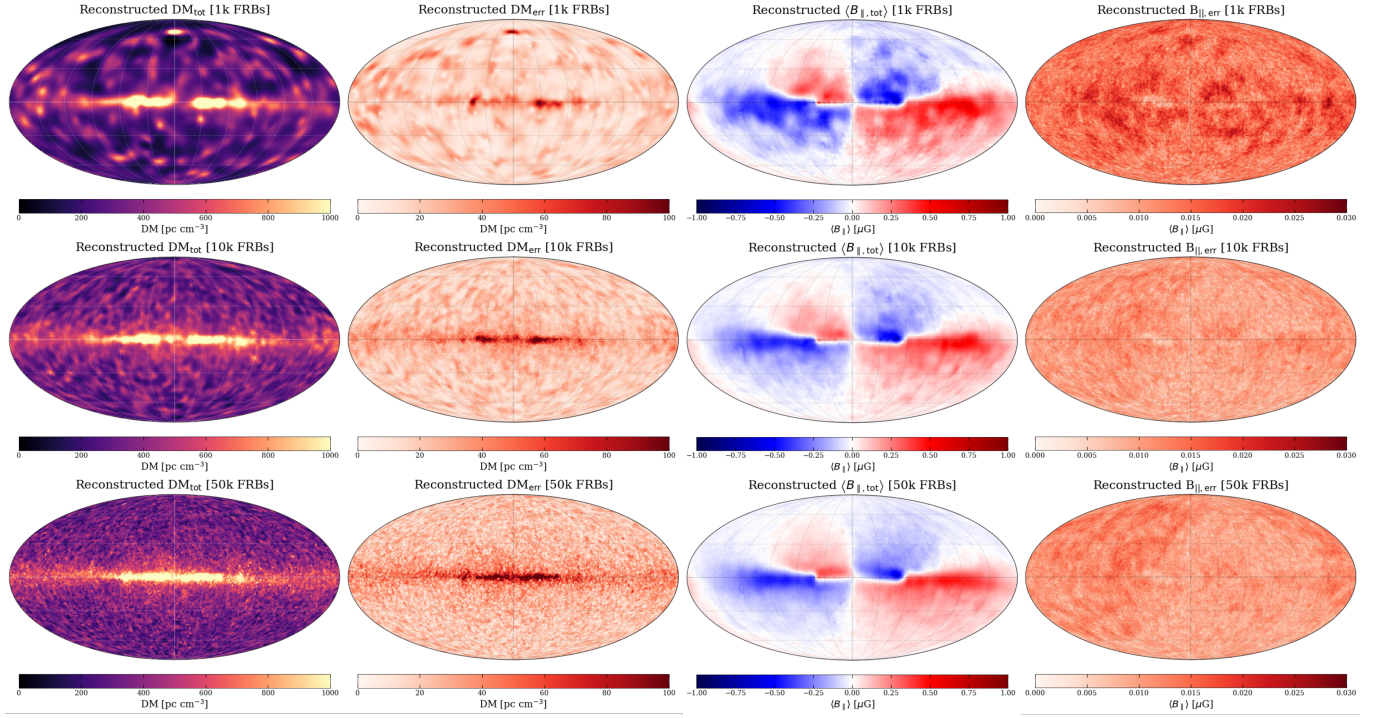
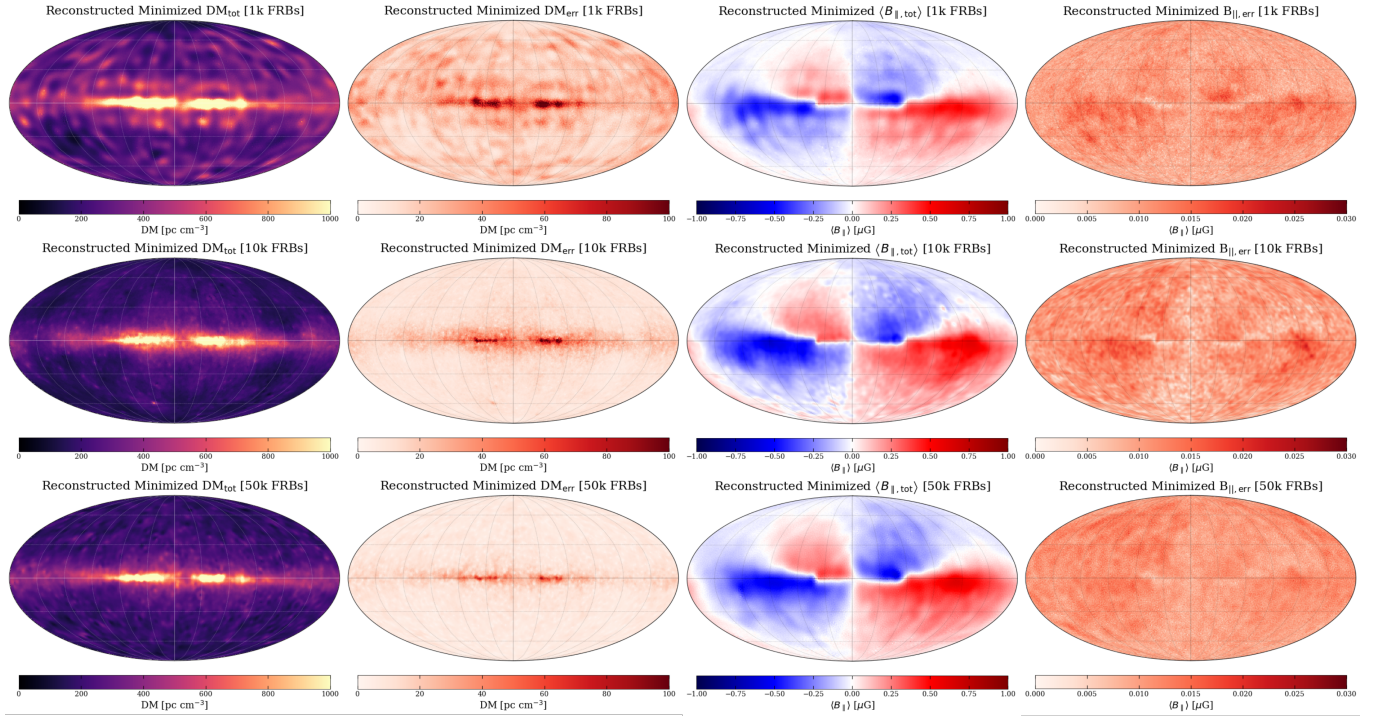


Figure A2. Full reconstruction outputs with errors corresponding to the result shown in Figure 4.





**Figure A3.** Identical setup to Figure A2 but corresponding to the results shown in the first two columns of Figure 5.



**Figure A4.** Identical setup to the previous two figures but corresponding to the results shown in the last two columns of Figure 5.



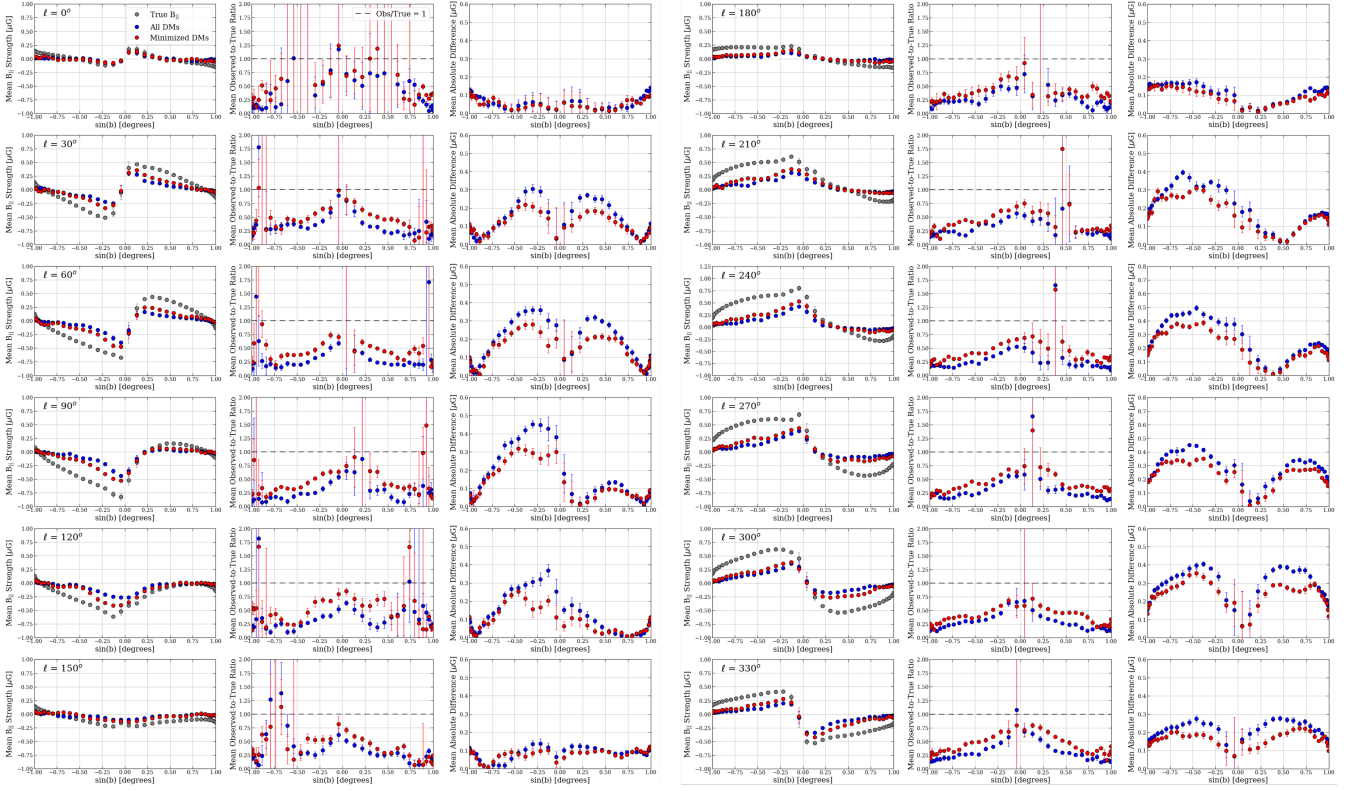


**Figure B1.** Analysis of the mean  $\langle B_{||} \rangle$  as a function of Galactic latitude at 30 deg intervals in the Galactic longitude. Expected results are plotted as grey circles, and reconstruction results are in blue (full data) and red (DM filtered data). For each slice in Galactic longitude, we show the mean  $\langle B_{||} \rangle$ , observed-to-expected ratio of  $\langle B_{||} \rangle$ , and absolute difference between expected and observed results, respectively.

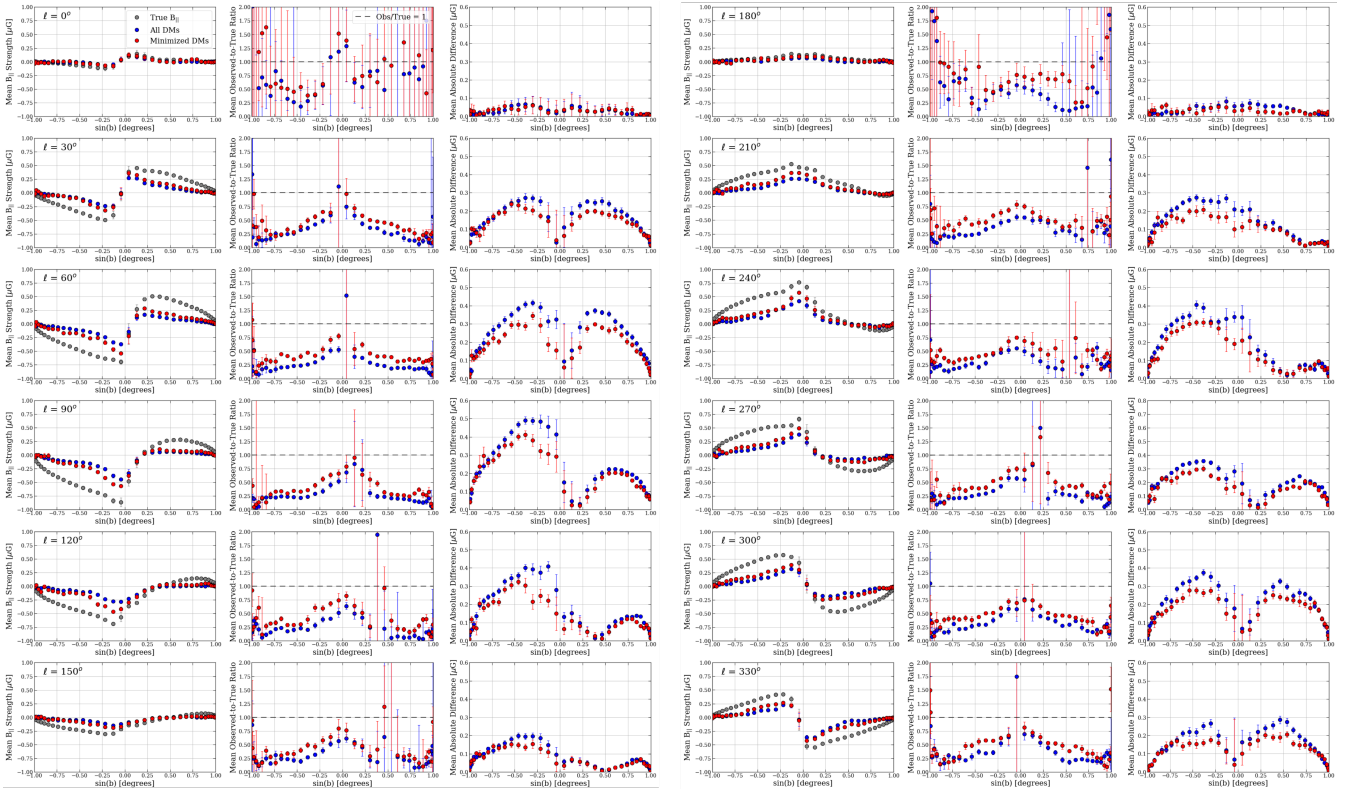


**Figure B2.** Same as Figure B1 but for the scenario without the X-shaped halo in the assumed GMF model.

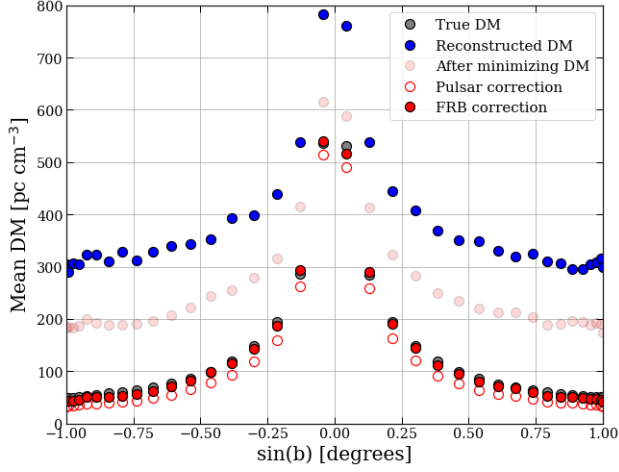


**Figure B3.** Analogous to Figure 9 without the X-shaped GMF halo.

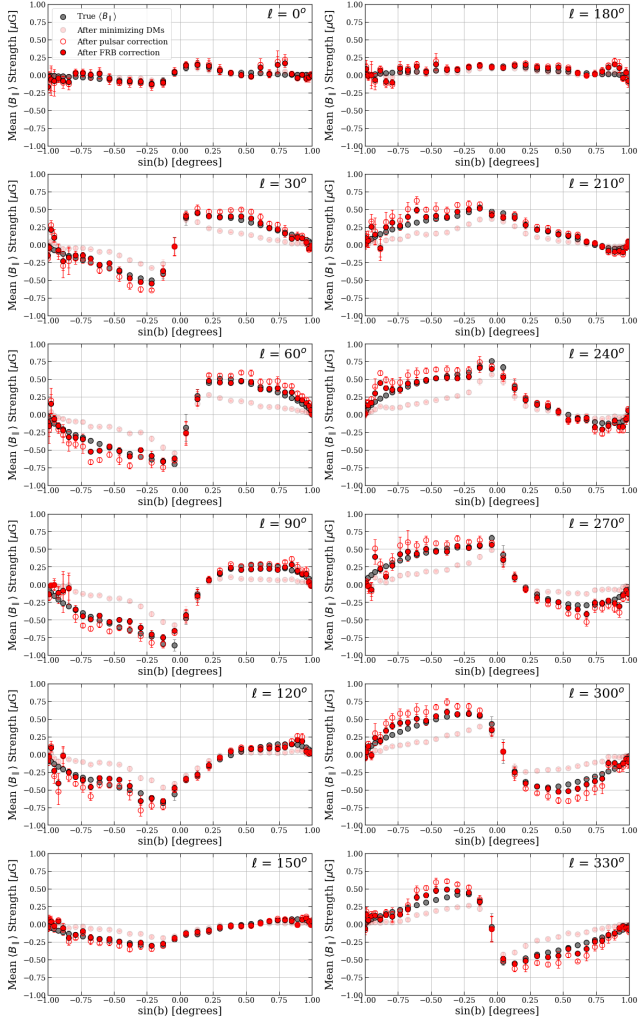


**Figure B4.** Analogous to Figure 10 without the X-shaped GMF halo.